**Forschungszentrum Karlsruhe**

**in der Helmholtz-Gemeinschaft**

**Wissenschaftliche Berichte**

**FZKA 6782**

# Alpha capture on $^{18}$O during stellar He burning

**Saed Dababneh**

Institut für Kernphysik

von der Fakultät für Physik und Astronomie
der Ruprecht-Karls-Universität Heidelberg
genehmigte Dissertation

**Forschungszentrum Karlsruhe GmbH, Karlsruhe**
**2002**

**Impressum der Print-Ausgabe:**

**Als Manuskript gedruckt**


**Forschungszentrum Karlsruhe GmbH**
**Postfach 3640, 76021 Karlsruhe**

**Mitglied der Hermann von Helmholtz-Gemeinschaft**
**Deutscher Forschungszentren (HGF)**

**ISSN 0947-8620**

**Abstract**

The $^{22}$Ne($\alpha$,n) reaction is the dominant neutron source for neutron capture nucleosynthesis ($s$-process) in massive stars and plays also a significant role for the $s$-process in thermally pulsing AGB stars. In these scenarios $^{22}$Ne is produced by the reaction sequence $^{14}$N$(\alpha,\gamma)^{18}$F$(\beta^+)^{18}$O$(\alpha,\gamma)^{22}$Ne. While the first reaction is well understood, $\alpha$-capture on $^{18}$O was affected by considerable uncertainties. At the temperatures of stellar He burning the reaction rate is determined by two resonances at $\alpha$-energies of 470 and 566 keV. Since these resonances were not yet successfully measured, the rates had to be based on estimated resonance strengths. In the present work the first direct measurement of the strengths of these extremely weak low energy resonances is reported. The use of a high-efficiency segmented Ge detector in coincidence with BGO counters covering a large solid angle led to a significantly improved experimental sensitivity, thus allowing for the clear identification of specific $\gamma$-transitions. As a result, resonance strengths of 1.0$\pm$0.2 $\mu$eV and 0.4$\pm$0.2 $\mu$eV could be obtained for the 566 and 470 keV resonances, respectively. When compared to the previously reported upper limits of $\leq$1.7 $\mu$eV, this result provides the basis for the reliable determination of the reaction rate during stellar He-burning. Accordingly, these data allow to reduce the uncertainties in the $s$-process neutron balance.

# Einfang von alpha-Teilchen am $^{18}$O während des stellaren He-Brennens


**Zusammenfassung**

Die $^{22}$Ne($\alpha$,n) Reaktion ist die Haupt-Neutronenquelle für die Elementsynthese durch Neutroneneinfang ($s$-Prozess) in massiven Sternen und spielt auch eine bedeutende Rolle beim $s$-Prozess in thermisch pulsierenden AGB Sternen. In diesen Szenarien wird $^{22}$Ne während des He-Brennens durch die Reaktionskette $^{14}$N$(\alpha,\gamma)^{18}$F$(\beta^+)^{18}$O$(\alpha,\gamma)^{22}$Ne erzeugt. Während die erste Reaktion gut verstanden ist, war der $\alpha$-Einfang von $^{18}$O mit beträchtlichen Unsicherheiten behaftet. Bei den Temperaturen im stellaren He-Brennen wird die Reaktionsrate von zwei Resonanzen bei $\alpha$-Energien von 470 und 566 keV bestimmt. Da diese Resonanzen bis jetzt nicht experimentell erfasst werden konnten, basieren die in $s$-Prozess-Studien verwendeten Reaktionsraten lediglich auf Abschätzungen der Resonanzstärken. In der vorliegenden Arbeit wird über eine direkte Messung der Stärken dieser extrem schwachen Resonanzen berichtet. Mit Hilfe eines Aufbaus aus einem hocheffizienten, segmentierten Ge Detektor in Koinzidenz mit BGO Zählern, die einen großen Raumwinkel abdecken, konnte die experimentelle Empfindlichkeit so weit verbessert werden, dass die für den $\alpha$-Einfang spezifischen $\gamma$-Übergänge eindeutig nachweisbar waren. Dadurch konnten die Resonanzen bei 566 und 470 keV erstmals vermessen und die Resonanzstärken mit 1.0$\pm$0.2 $\mu$eV, beziehungsweise 0.4$\pm$0.2 $\mu$eV, bestimmt werden. Im Vergleich zu den bisherigen Obergrenzen von $\leq$1.7 $\mu$eV ergibt sich jetzt die Möglichkeit, die Reaktionsraten im stellaren He-Brennen zuverlässig festzulegen und so die Unsicherheiten bezüglich der Neutronenbilanz im $s$-Prozess zu reduzieren.

# Contents

# List of Tables

# List of Figures

# Chapter 1

# INTRODUCTION

## 1.1 Preamble

One of the fundamental problems of astrophysics is the quest for the origin of the chemical elements. The ashes of the Big Bang consist predominantly of hydrogen and helium. After the formation of galaxies these ashes are subsequently burned in the stellar interiors. All elements up to the region of the iron group can be synthesized in such environments by charged particle induced nuclear reactions (hydrogen burning, helium burning, etc..). These reactions are increasingly impeded by the Coulomb barrier, a fact that explains the sharp drop in the elemental abundances from $A$ = 12 to $A$ = 50 [Rol88]. Ultimately, silicon burning gives rise to the clear abundance peak at $A$ = 56 where the most stable nuclei are produced. Further build-up of much heavier nuclei by charged particle reactions is strongly inhibited due to the strong Coulomb barrier as well as the decreasing binding energy per nucleon [Käp99].

Beyond the iron peak, the observed abundance distribution of the heavy elements exhibits a much slower decrease with mass number, the abundances being much higher than expected from charged particle induced reactions. In this region, the existence of several twin peaks in the abundance distribution associated with neutron shell filling at the magic neutron numbers ($N$ = 50, 82 and 126) led to the extension of nucleosynthesis in stars by neutron capture, which is obviously unaffected by Coulomb repulsion. These twin peaks are the signature of the slow ($s$) and rapid ($r$) neutron capture processes. Both processes provide about 50% of the observed heavy element abundances.

The $r$-process occurs in regions of extremely high neutron densities, presumably during stellar explosions in type II supernovae, where the neutron capture times are so short, compared to $\beta$-decay, that neutron-rich nuclei far off stability can be reached. Attempts to describe the $r$-process are hampered by the large uncertainties in the nuclear physics data far from stability and by problems related to detailed modeling of stellar explosions ([Käp99] and references therein).

On the contrary, the $s$-process operates at relatively low neutron densities

and the neutron capture times are much longer than typical $\beta$-decay half-lives. Therefore, the *s*-process reaction path follows the stability valley. The developing *s* abundances are determined by the respective (n,$\gamma$) cross sections, such that isotopes with smaller cross sections build up larger abundances. This explains the above mentioned peaks in the abundance distribution corresponding to neutron shell filling at the magic numbers. Since (n,$\gamma$) cross sections for those mainly stable nuclei can be measured in laboratory experiments, a large pile of data led to a fairly quantitative picture of the *s*-process.

An important remaining problem for our understanding of *s*-process nucleosynthesis is the quest for the efficiency of the neutron producing reactions that are feeding the neutron capture chains in these scenarios.

## 1.2 Neutron sources for the *s* process

It was as early as 1957 when the product of the stellar neutron capture cross section times the *s* abundance $<\sigma(A)>N_S(A)$ was identified by E.M. Burbidge, G.R. Burbidge, W.A. Fowler and F. Hoyle ($B^2FH$) as the characteristic quantity of the *s* process [$B^2FH57$]. The concept of this canonical approach has been meanwhile impressively confirmed, in particular by the quantitative description of the abundances of the so-called *s*-only nuclei, which can be unambiguously assigned to a pure *s* process origin [Käp99]. From a comparison between calculated $<\sigma>N_S$ values and the corresponding empirical products for the *s*-only nuclei, at least two different *s* process components can be inferred; these are the "main" and the "weak" components [Käp89, Käp99]. These two components indicate that two separate sites contributed to the abundance of *s*-nuclei. The weak component is believed to be related to the production of nuclei up to Zr ($A$ < 90) during He burning in the cores of massive stars ($\geq$15 $M_\odot$), while the main component ($A$ = 90 to 209) is likely to occur in the He burning shell in low mass stars [Mey94, Gal98].

The $^{22}$Ne($\alpha$,n) neutron source plays an important role in both scenarios.This reaction completely dominates the neutron production in massive stars. On the other hand, the lower temperatures in low mass stars favor the $^{13}$C($\alpha$,n) reaction that provides about 95% of the total neutron exposure. However, the final abundance patterns are modified in a characteristic way by the marginal activation of the $^{22}$Ne($\alpha$,n) reaction at the end of each neutron production episode in thermally pulsing AGB stars [Gal98]. At this evolutionary stage, recurrent He shell flashes lead to sufficiently high temperatures of T ~ $3\times10^8$K ($T_9$ ~ 0.3) that $^{22}$Ne($\alpha$,n) reactions add 5% to the total exposure, but at a much higher neutron density than in the previous $^{13}$C($\alpha$,n) phase.

Accordingly, the abundance patterns that we observe are strongly influenced by the $^{22}$Ne($\alpha$,n) neutron source. It is this interplay between the complementary neutron sources, $^{13}$C($\alpha$,n) and $^{22}$Ne($\alpha$,n), which represents a persisting

challenge for nuclear astrophysics since both reactions are yet uncertain due to lack of data in the relevant temperature regions of the respective stellar sites.

This work is devoted to an improved study of the reaction sequence leading to the build-up of $^{22}$Ne during stellar He burning.

In the earlier CNO cycle during core hydrogen burning in massive stars, practically all of the CNO nuclei are transformed into $^{14}$N since proton capture on $^{14}$N is the slowest reaction in the cycle [Rol88]. After hydrogen exhaustion, the core contracts until its density and temperature are sufficient for helium burning to be ignited. In this stage of stellar evolution, the main energy source is the triple $\alpha$ reaction. The $^{14}$N ashes of hydrogen burning are now converted to $^{22}$Ne by the reaction sequence $^{14}$N($\alpha$,$\gamma$)$^{18}$F($\beta^+$)$^{18}$O($\alpha$,$\gamma$)$^{22}$Ne. The resulting $^{22}$Ne abundance and hence the efficiency of the subsequent $^{22}$Ne($\alpha$,n)$^{25}$Mg neutron source for the *s* process thus depends on the preceding $\alpha$ capture reactions on $^{14}$N and $^{18}$O. The reaction rates at the temperatures of core helium burning are expected to be dominated by contributions of low energy resonances [Käp98]. While the first reaction is well understood [Gör00, Gör01], $\alpha$-capture on $^{18}$O is still affected by considerable uncertainties.

## 1.3 $\alpha$-capture on $^{18}$O

Previous direct measurements of the $^{18}$O($\alpha$,$\gamma$)$^{22}$Ne reaction covered the energy range from 0.6 to 2.3 MeV [Tra78] and from 2.15 to 3.70 MeV [Ada69]. Therefore, the stellar reaction rate is well determined by the available experimental data at temperatures $T_9$=0.3-4.3. At the relevant *s*-process temperatures ($T_9$<0.3), however, the rate might be significantly enhanced if additional resonances could be detected at energies below 600 keV [Rol88, Tra78]. At these energies, penetration through the Coulomb barrier reduces the $\alpha$-width ($\Gamma_\alpha$) sharply to values much less than the $\gamma$-width ($\Gamma_\alpha \ll \Gamma_\gamma$). Since the resonance strength is defined by the product of the statistical factor $\omega$ and the width ratio $\gamma = \Gamma_\alpha\Gamma_\gamma/(\Gamma_\alpha+\Gamma_\gamma)$, the strength of these low energy resonances depends only on $\Gamma_\alpha$. It was indicated [Tra78] that due to the $\omega\gamma = \omega\Gamma_\alpha$ dependence and due to the barrier penetration factor contained in $\Gamma_\alpha$, the low energy resonances were inaccessible to the experiments aiming at a direct strength measurement. These possible resonance levels, that would dominate the reaction rate at astrophysical energies, have been so far studied only indirectly. The $^{18}$O($^6$Li,d)$^{22}$Ne $\alpha$ transfer reaction has been used to investigate the level structure of $^{22}$Ne around the $\alpha$-threshold [Gie94]. Attempts to measure these low energy resonances directly could provide only upper limits for the resonance strengths [Vog90, Gie94]. The predicted resonance strengths are low ($\leq$1.7 $\mu$eV) and are again reported as extremely difficult to be accessed in direct measurements [Käp98].

In general, there is a strong demand for reliable charged particle reaction rates for stellar nucleosynthesis calculations. The main problem is that these

measurements are handicapped by high backgrounds, which include natural, cosmic ray induced, as well as beam induced components. Background reduction and event suppression techniques are thus imperative for the investigation of extremely weak reactions [Wie01].

This work attempts to meet these requirements. In order to improve the gamma detection sensitivity, or in other words to improve the capture yield-to-background ratio, different event suppression methods have been considered.

The method concentrates on particular features of the cascade transitions that distinguish them from the background. With standard spectroscopy, background levels even with heavy passive shielding are overwhelmingly much higher than the expected yield from the weak resonances. Thus, after careful understanding of the different components in the background spectrum and of the expected transitions in the $^{22}$Ne compound nucleus, the setup has been designed to selectively exclude all events that do not satisfy certain physical criteria characteristic of the sought transitions. Since the decay of the resonant state, unlike common backgrounds, includes cascades of well defined $\gamma$-lines, the corresponding coincidence spectra selectively contain the desired information with substantial background elimination. The method utilizes high efficiency BGO scintillators and high resolution granular Ge detectors from which all information is recorded event by event for later off-line analysis.

As a result, we were able to significantly enhance the detection sensitivity to a degree that enabled the direct identification of at least the first excited state to ground state transition in the compound nucleus $^{22}$Ne for the extremely weak resonances in the capture reaction.

This direct measurement provides the important resonance strengths for $\alpha$-particle energies below 600 keV, and consequently a more accurate determination of the stellar reaction rate.

# Chapter 2

# EXPERIMENTAL TECHNIQUES AND DATA REDUCTION

## 2.1 General features

The experiment has been conducted at the 3.7 MV Van de Graaff accelerator facility of the Institut für Kernphysik, Forschungszentrum Karlsruhe. Proton- and alpha-beams, guided through a Ta-collimator and a $LN_2$-cooled Cu trap, were swept horizontally and vertically across an effective target area of 1 $cm^2$ to illuminate the target homogeneously. In the final measurement of the low energy resonances, targets were mounted at $0^o$ to the beam direction and were directly water cooled. Target and chamber formed a Faraday cup for measuring the integrated beam current on target. A negative voltage of 300 V was applied to the Cu trap tube to suppress secondary electron emission. Detailed description of the experimental setup and data reduction procedures, gamma detection system, targets and target stability as well as background suppression will follow in the subsequent sections of this chapter. The coincidence calculations and all related aspects will be discussed thoroughly in conjunction with the results of the $^{18}O(\alpha,\gamma)^{22}Ne$ measurements (Chapters 3 & 4).

### 2.1.1 Experimental setup

The experimental setup was optimized in several steps and was eventually adopted in the version sketched in Fig. 2.1. Alpha particle beams of 50-120 $\mu$A were used to irradiate $Al_2{}^{18}O_3$ targets of high stability (see Section 2.4). $\gamma$-rays from capture reaction on $^{18}O$ were detected by a high purity Ge-detector array in clover geometry (Fig. 2.2) as well as by a large solid angle array of BGO scintillators for the coincident detection of $\gamma$-ray cascades. Backgrounds were minimized by a heavy lead castle combined with large area plastic scintillator panels for secondary cosmic-ray suppression.

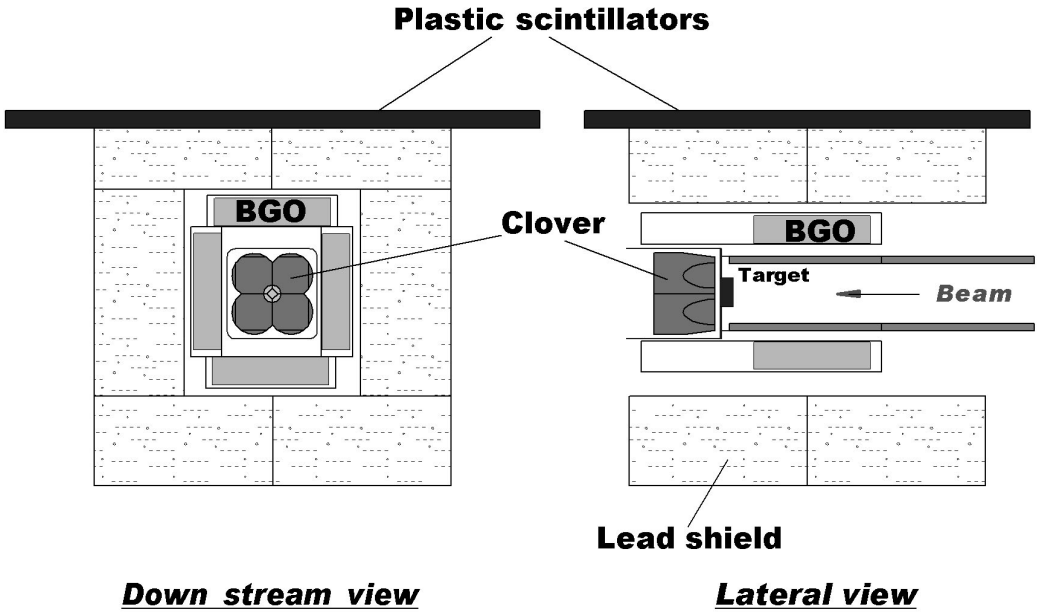


**Figure 2.1: Downstream and lateral views of the experimental setup are represented schematically. The cold trap inside the beam line is omitted for better readability of the figure. While the lead shield and all detectors are to scale, the beam tube and the target are emphasized. After several test geometries, this final setup has been ultimately adopted to search for the weak low-energy resonances in the $^{18}$O($\alpha$,$\gamma$)$^{22}$Ne reaction. Energy windows have been set in the BGO spectra to look for cascade coincidences detected in the Clover Ge-array. The plastic scintillators have been used to exclude events that correspond to secondary cosmic-ray interactions in the Clover-BGO assembly or in the passive shield.**

The main component in the gamma detection system is the Eurisys Mesures Clover array (Fig. 2.2). It consists of four coaxial n-type HPGe diodes of 50 mm diameter and 70 mm length cut in a way (Section 2.2) that enables close packing with a Ge-Ge distance of only 0.2 mm. The crystals are mounted in a common cryostat. The total active Ge volume is $\sim$ 470 cm$^3$ [Duc99, Jos97], which results in an absolute efficiency in close geometry of $\sim$ 7% at 1 MeV $\gamma$-ray energy.

The second part of the $\gamma$-detection system consists of four Scionix BGO (Bismuth Germanate $Bi_4Ge_3O_{12}$) crystals, 13$\times$13$\times$3 cm in size, surrounding the upstream side of the target. This is a high Z, high density material considered as an efficient $\gamma$-ray absorber. The BGO detectors together with the plastic

**Figure 2.2: Close packing of the four Ge crystals in a Clover detector.**

scintillator panels on top of the setup ($60\times50\times2$ cm) serve to provide coincident hits that can be used to suppress the Clover signals according to different criteria. These active detectors were used, for example, in cosmic-ray and Compton suppression as well as for identifying coincidences between the Clover and signals in corresponding energy windows of the BGO spectrum. The passive lead shield consisted of a 10 cm thick layer for reducing the ambient $\gamma$-ray background level.

The geometry of the final setup has been optimized for Clover-BGO coincidences, as Compton suppression was found to be not as important according to a preliminary test measurement (Subsection 3.2.1). The Clover Ge detector covers forward angles and the BGO scintillators are oriented so that they cover a large solid angle upstream the $^{18}$O target. The final geometry adopted for the experimental setup as sketched in Fig. 2.1 has been modeled in detail for extensive Geant4 Monte Carlo simulations which are described in Section 2.2.

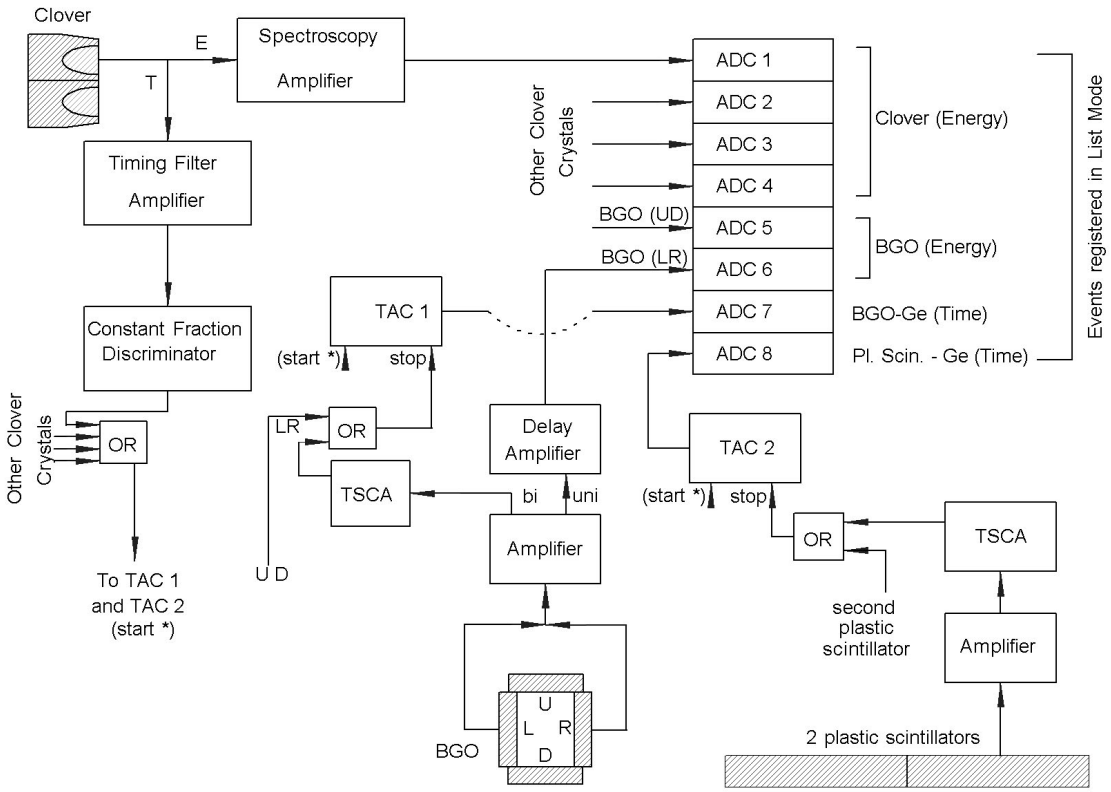


**Figure 2.3: Schematic representation of the data acquisition system.**

### 2.1.2 Data acquisition and data analysis software (LiMDA)

The signals from all detectors, i.e. the timing and energy outputs of the four Clover crystals, the timing and energy outputs of the four BGO scintillators (pairs of two coupled together) as well as the timing signals from the two plastic scintillators are processed as shown schematically in Fig. 2.3. The signal processing is intended to record all relevant energy and timing information for later off-line treatment. For this particular reason, no hardware vetos have been included, so that all necessary information is preserved for repeated and flexible software analysis.

The data acquisition system consists of eight amplitude-to-digital converters (ADC):

**ADC 1,2,3, and 4 are used for the four Clover energy outputs.**
**ADC 5 and 6 are used for the two pairs of coupled BGO energy outputs.**
**ADC 7 is used for the Ge-BGO timing signals.**
**ADC 8 is used for the Ge-plastic scintillator timing signals**

All events are recorded in list mode: If a hit is registered in any ADC, all other ADC's are read within a specified coincidence time and the whole sequence is

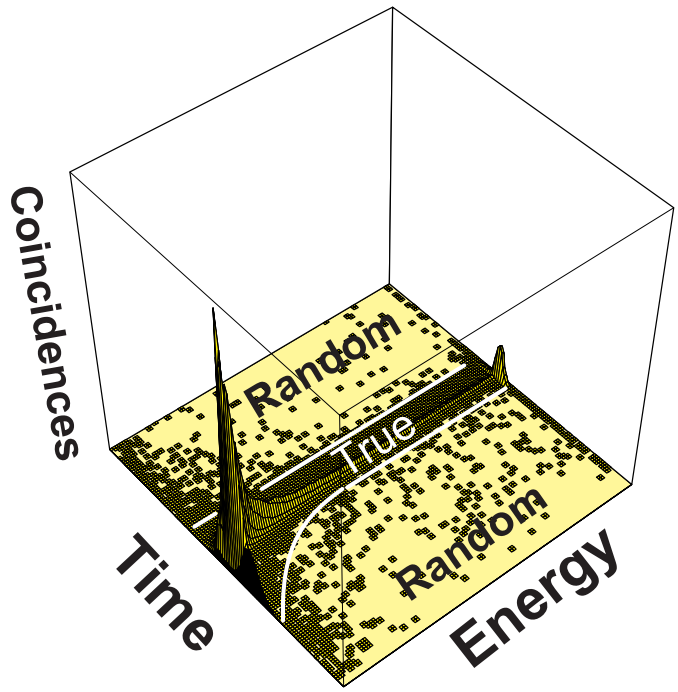


**Figure 2.4: Elimination of "Random" and reserving "True" Clover-BGO coincidences in a band defined by the time resolution of the setup.**

stored. The final list file thus consists of blocks (called events) of eight registers per event representing the eight ADC converted digital outputs. Obviously, an event could contain one or more firing ADC's but non-firing ADC's are also registered. In this way, one event consists of 8 words (16 byte) and each 2-byte word is related to one single ADC where the lower 13 bits register the channel number (corresponding to 8k analog-to-digital conversion) and the higher 3 bits give the ADC number. The desired composite spectra are then generated offline using a special software (***Li***st ***M***ode ***D***ata ***A***nalysis **LiMDA**) written for this purpose.

From each single list file, and using the proper energy calibration for each individual crystal, different (suppressed and unsuppressed) addback or direct spectra (Section 2.3.1) can be generated and analyzed in a flexible way. To build the total addback or direct spectrum, the first four words in an event which correspond to the four Clover energy outputs are used. The segmentation of the Ge Clover detector allows the reconstruction of an original $\gamma$-ray if the Compton scattered photon or the annihilation photons following pair production are detected in one or more of the neighboring Ge crystals. This so-called addback mode results in an increase of the overall detection efficiency. The other four words can be used to suppress the events according to different criteria defined

by the user. The unsuppressed Clover spectrum can be generated simply by ignoring the BGO and the plastic scintillation bytes in the binary list file events. The anticoincidence and/or the coincidence spectra with any combination of scintillation bytes can also be generated.

In each kind of calculation, the defined criteria given as an input to the code are first used to reduce the original list file. This reduced list file is then analyzed. In addition to the single crystal spectra, the analysis includes the spectra for each multiplicity, for the total addback and direct modes, as well as for partial addback used for Doppler correction (Section 2.3.3). The BGO energy spectra that satisfy the same reduction criteria are also generated.

The above mentioned suppression criteria could include energy windows in the BGO spectra. This is especially useful when the coincidence calculation is intended to search for a $\gamma$-line which is part of a cascade. For example, the BGO energy window can be set to include the expected primaries in that cascade. This clearly helps in minimizing background in the coincidence Clover spectrum. Further background reduction can be accomplished by additional suppression using the plastic scintillator signals. Thus, Clover-BGO energy-window coincidences which are in anticoincidence with the plastic scintillators are used to define the cascade events from the $^{18}$O$(\alpha,\gamma)$ reaction.

The non-cosmic background component in the coincidence spectra can be even further reduced. This is the random coincidence component. In order to minimize Ge-BGO random coincidences, 3D plots have been prepared as part of the list file analysis software LiMDA which show the number of coincidences as a function of both energy and time. Fig. 2.4 is an example. In the suppressed spectrum, only events inside a 'band', labeled 'True' in the figure, are used in the event reduction. This band is defined in the high energy part to be slightly wider than the time resolution of the system which is about 12 ns. The clear "walk" produced by the low pulse-height Ge signals widens the band at low energies. All Ge-BGO coincidence events outside this band are considered as random and the corresponding Ge raw data are treated as having no BGO coincidences. In the case of cosmic suppression, and since there are only time signals registered in the list file, a simple rectangular strip in the TAC output spectrum is used to distinguish between random and true events. Depending on the suppression criteria of coincidence (anticoincidence) analyses, the software keeps (rejects) events with "true" coincidences in the newly generated suppressed temporary list file.

Another possible calculation integrated in LiMDA is worth mentioning here. If we consider the whole assembly consisting of the Clover and the BGO's as one calorimeter, then a Q-value energy window can be set where events are registered in the suppressed list file only if the total energy deposition in the calorimeter lies within this window. This method will be compared to the BGO energy-window coincidence calculation and to Compton suppression when applied to resonances in the $^{18}$O$(\alpha,\gamma)^{22}$Ne reaction (Subsection 3.2.1).

On the contrary to the BGO window suppression, an energy window can also be set for the Clover addback spectrum as a suppression criterion. This not only provides the coincident BGO spectra, but can be used to test summation effects in the Clover itself. If the window is set around a $\gamma$-line in the Clover addback spectrum, the direct mode Clover spectrum obtained from the reduced list file contains information about lower energy gammas that sum into the specified window. Naturally, this includes Compton continua in addition to annihilation photons and escape peaks. Any other lines distinguished in the spectrum are clearly members of a cascade and the calculation of the yield of the $\gamma$-line in the window should take this summation contribution into account.

Finally, the above mentioned analysis provides information, for any single line, about the contribution of "summing-in" effects. As an alternative analysis that takes into account the "summing-out" effects, the desired energy window can be set in LiMDA on individual Clover crystals instead of the total addback spectrum. The resultant addback calculation of multiplicities $\geq 2$ obviously provides the spectrum of events summing out of the window set on the single crystal energy spectra.

Table 2.1 summarizes the different possibilities of event suppression included in LiMDA. For each single temporary list file generated in any kind of suppression, all spectra corresponding to the different Clover modes of operation are generated. Examples illustrating these calculations will be provided throughout the text.

**Table 2.1: Event suppression processes included in the LiMDA code. For each kind of suppression, all Clover modes of operation are considered.**

| ***Type of Suppression*** | | ***Comments*** |
|---|---|---|
| *No suppression* | | Scintillation data ignored |
| *Anticoincidences:* | | |
| | Cosmic suppression | Use plastic scintillator data |
| | Compton suppression | Use BGO data |
| *Coincidences:** | | |
| | Q-value | Window on Clover + BGO |
| | BGO window | Cascade coincidences |
| | Clover addback window | Direct mode gives "summing-in" |
| | Clover crystal window | Addback (M$\geq$2) gives "summing-out" |

** With or without cosmic suppression.*

## 2.2 Geant4 Simulation

The Geant4 object oriented simulation toolkit [GEANT4] which uses the Monte Carlo technique to simulate the experimental setup and response of differ-

ent detectors has been tested first by comparing the simulated response of a single Ge crystal to the experimental results. This comparison, which shows remarkable agreement, provides confidence in the subsequent simulations for the different modes of operation of the composite setup.

In order to simulate the performance of the main detection unit, the rather complex Clover geometry was carefully modeled. For example, the bevels at the front face of each Ge crystal generate, on two sides, a semi-elliptic surface. The other two sides of each crystal are mostly flat to allow for the close packing with the adjacent crystals. The front face of the crystal has thus a quasi-square shape while its rear face is quasi-circular since two sides in the back half conserve the 50 mm diameter of the original Ge cylinder. These details had to be considered in the simulation.

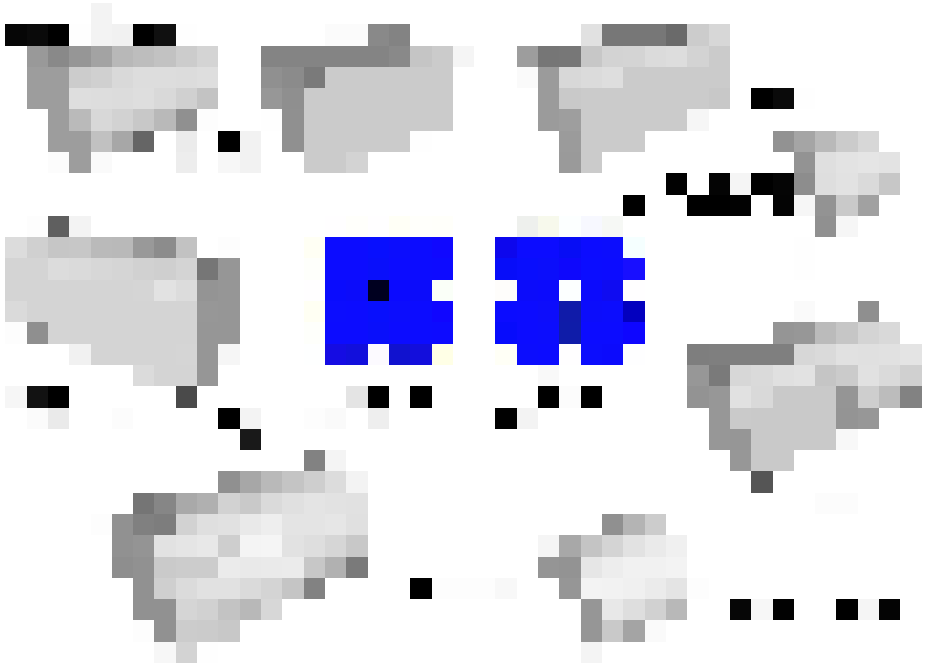

**Figure 2.5: Virtual reality (VRML) visualization of the Boolean construction of Clover crystals for detailed Geant4 simulations.**

A significant feature in Geant4 is the ability to do Boolean operations on standard solids called CSG (Constructed Solid Geometry) to produce more complex shapes. These Boolean operations like “Union” and “Intersection” on standard geometrical volumes (Box, Cylinder, Cone) have been used as described in Fig. 2.5 to reproduce the first Clover crystal. The concept of “positioned” volumes, useful for saving memory when describing complex or repeated struc-

tures, has been used to build the other three crystals ending up with the complete geometry of the Clover. This procedure ensures preserving the shape and dimensions of the crystals. In this simulated volume, the coaxial hole of each diode as well as the dead material were included. The whole structure is then mounted in a 1.5 mm thick aluminium can. The space between the Al box and the crystals is 'filled' with vacuum.

The BGO scintillators and their aluminium housing as well as the other components in the setup are rather more straightforward to reproduce. The 0.4 mm Ta target backing, the target holder, the Cu cold trap and the beam line which act as absorbers and scatterers between the target and both types of detectors were also carefully structured. The passive lead shield is finally added as well.

The simulation is of course intended to track the $\gamma$-rays produced in the target. Therefore room and cosmic backgrounds were not included in the simulation. Accordingly, the plastic scintillators above the passive shield were not defined in the simulation.

The beam spot on target, which is about 1 cm in diameter, has been simulated by defining the gamma "source" to be distributed randomly in a perpendicular two-dimensional plane at the target position.

The energy deposited in each Ge and BGO volume is then collected and histogrammed to obtain the relevant spectra. In addition, the original data can be manipulated to obtain all desired combinations of hits. The "addback" and "direct" spectra of the Clover represent a simple example. All kinds of event suppression described in the previous section are also implemented.

The detection efficiencies obtained from the simulation are presented and compared to experimental results in the following section.

## 2.3 Gamma detection system

The detailed description of the detection system given in this section summarizes the experimental observations together with those obtained from the Geant4 simulations. To start with, the main features of the Clover spectra as well as its different modes of operation are discussed, illustrating their advantages and drawbacks.

### 2.3.1 The Clover detector: Features and modes of operation

Events in the Clover detector registered in list mode as described in Section 2.1 may exhibit different 'multiplicities'. Multiplicity 1 means a hit in one crystal with no coincident hits in any other. Multiplicities 2, 3 and 4 correspond to simultaneous hits detected in 2, 3 or 4 crystals, respectively, due to Compton scattering or pair production.

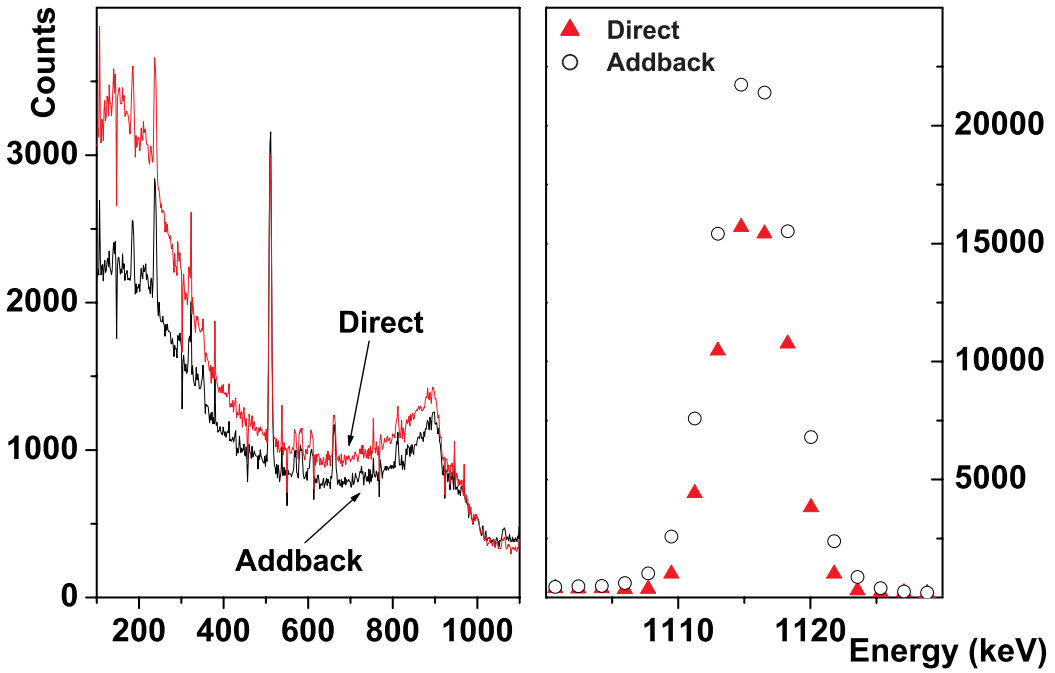


**Figure 2.6: The 1115 keV line of the $^{65}$Zn source along with its Compton continuum, both in addback and direct mode. The addback gain in peak efficiency is illustrated in the expanded part of the spectrum containing the full energy peak (right panel). The corresponding Compton scattered photons restored to the full energy peak in addback mode result in a clear reduction of the Compton continuum (left panel).**

If each crystal in the Clover detector is considered independently as a single detector, even if the multiplicity was higher than 1, then the composite Clover detector is said to be operated in the 'direct' mode. Thus the photopeak detection efficiency is simply the sum of the individual photopeak efficiencies of each of the four crystals.

On the other hand, the close packing of the Clover detector facilitates its operation in the so called 'addback' mode. In this mode, coincident events in different crystals are summed (energy sum) resulting in the reconstruction of full-energy signals if Compton-scattered and 511 keV annihilation photons escaping from one crystal are detected in another crystal. The summed signals are stored in the addback spectrum, which results in improved full energy peak efficiency on the expense of the Compton continuum and escape peaks. Fig. 2.6 illustrates the photopeak efficiency gain of a factor $\sim$ 1.6 in addback mode at 1115 keV ($^{65}$Zn source) and the corresponding reduction of the Compton continuum. Fig. 2.7 shows the contribution of different multiplicities to the

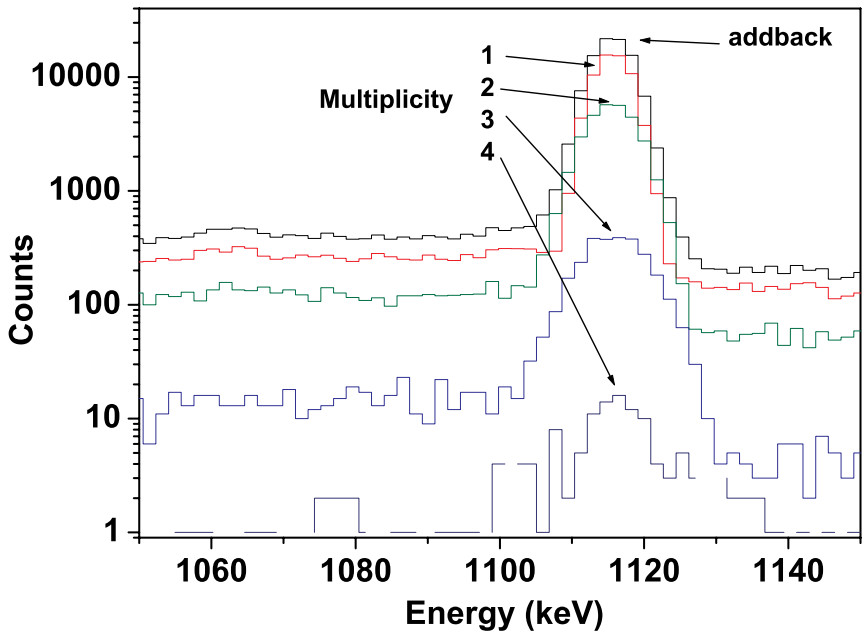


**Figure 2.7: The contribution of different multiplicities to the photopeak in the total addback spectrum of Fig. 2.6.**

full-energy peak. The measurement was conducted with the $^{65}$Zn source placed in the position of the $^{18}$O target.

At high gamma energies, pair production prevails and the annihilation photons detected simultaneously in other crystals are restored in the full energy peak. This effect is demonstrated in Fig. 2.8 which shows the high energy part of the gamma spectrum obtained on top of the 750 keV resonance of the $^{18}$O($\alpha$,$\gamma$)$^{22}$Ne reaction. The transfer of counts from the escape peaks to the full-energy peak by detection of annihilation photons in another crystal is quite obvious. The detection efficiency for the full-energy, single-escape and double-escape peaks in addback and direct mode will be discussed in detail later in this chapter.

The disadvantage of the addback mode becomes clear in case of coincident cascade photons resulting from subsequent transitions especially in the decay of a highly excited nuclear state. Summing effects complicate the intensity calculation where the observed yield depends not only on the detection efficiency for monoenergetic gammas but on the possibility of detecting coincident cascade photons as well. In such a case, however, the detector can be operated in the direct mode. This summing effect can be easily seen in Fig. 2.8 where the forbidden transition from the resonant $0^+$ state to the $0^+$ ground state is seen

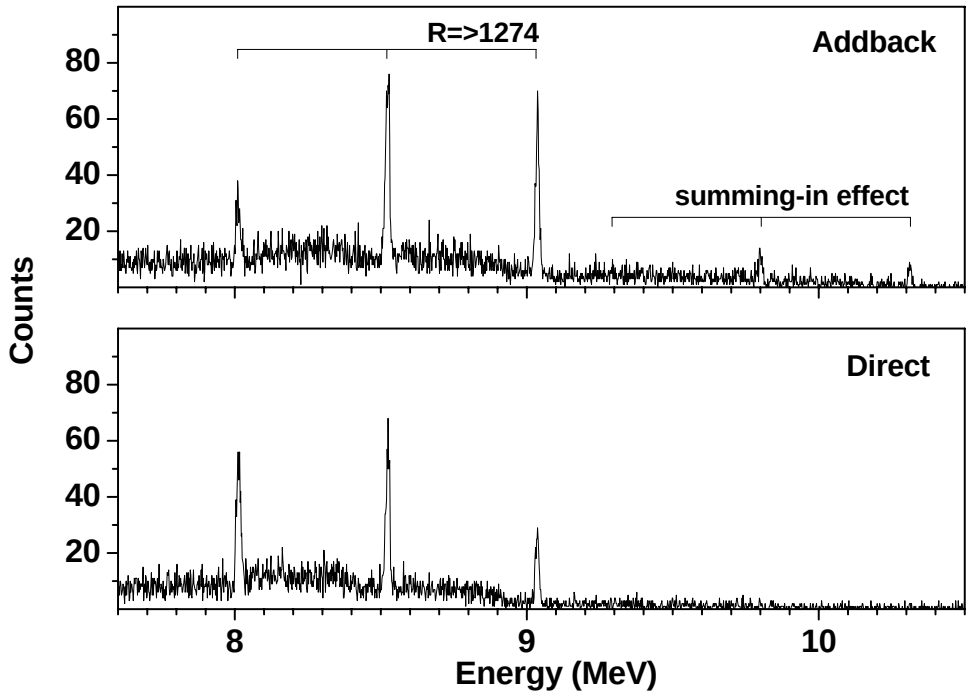


**Figure 2.8: High energy part of the spectrum acquired on top of the 750 keV resonance of the $^{18}$O($\alpha$,$\gamma$)$^{22}$Ne reaction, both in addback and direct mode. The gain in the full energy peak is clear in addback mode while the summing effect is illustrated by the appearance of the forbidden transition to the ground state.**

clearly only in addback mode. This drawback in addback calculations makes it necessary to correct for losses in photopeak efficiencies. The observed efficiency at a given energy and for the same geometry is affected by the probability for detecting a coincident cascade photon as well as by its angular correlation. This issue will be dealt with quantitatively in the following subsection. Partial addback and direct calculations could help, however, in correcting for Doppler broadening as explained in Subsection 2.3.3.

The generation of the full addback spectrum from the raw list file data involves as a first step the summation of the first four energy-calibrated single words which correspond to the four Clover crystals. The results are then histogrammed with a bin width that corresponds to the average energy per channel number for the four crystals. The addback spectrum obtained in this manner might need rebinning in order to statistically redistribute the energy sum. This is especially useful for features related to low yield peaks in the spectrum. The rebinning calculation is designed as follows: First, normal (Gaussian) random numbers are generated with zero as their average value and unity as their stan-

dard deviation (for example 0.12, 1.23, -0.33, 0.34, -1.76, ...). These random numbers are then digitized (0, 1, 0, 0, -1...) to produce the "channel" shift. The rebinning has been applied to the coincidence spectrum in search for the 470 keV resonance of the $^{18}$O($\alpha$,$\gamma$)$^{22}$Ne reaction where the 1274 keV peak feature is extremely weak (Fig. 4.6).

### 2.3.2 Clover detection efficiency in different modes

As a starting point, the detection efficiency of the Clover detector in the standard geometry without cascade event suppression (only cosmic suppression) is first investigated. For this purpose a (p,$\gamma$) reaction with a strong resonance that yields several $\gamma$-rays over a large energy range [Sco75] is considered. The 992 keV resonance in the $^{27}$Al(p,$\gamma$)$^{28}$Si reaction has been used for the efficiency calibration of the Clover detector, both in addback and direct modes. To achieve this, a list file acquired on top of the 992 keV resonance for a total charge of 2.5 mC on a 22 keV thick Al target has been analyzed. This target thickness is more than sufficient to stop all recoils, and yet ensures that nearby resonances are not excited, the nearest resonance being at 937 keV [End90]. The relative intensities of the $\gamma$-lines are taken from [Ant77]. The detection efficiency is calculated using the relation:

$$Y_\infty = \frac{N_A}{A}\varepsilon\frac{\lambda^2}{2}\omega\gamma\frac{M+m}{M}\frac{1}{T(E)}I_\gamma, \tag{2.1}$$

where $T(E)$ is the stopping power of the target, $I_\gamma$ the relative intensity of the respective $\gamma$-line and $Y_\infty$ is the maximum observed yield (per incident proton) at the plateau of the thick target excitation function. By adopting the resonance strength of $\omega\gamma = 1.91 \pm 0.11$ eV [Pai79], the absolute detection efficiency is calculated using the relation

$$\varepsilon = \frac{Y_\infty}{1.7654 \times 10^7 I_\gamma}. \tag{2.2}$$

The resulting experimental Clover efficiency data together with that obtained from the Geant4 simulation for full energy, single escape and double escape peaks in both direct and addback modes are shown in Fig. 2.9. The remarkable agreement between experiment and simulation in direct mode provides confidence in the efficiency calibration in this mode. All the observed experimental efficiency values for addback mode lie, on the other hand, below the monoenergetic efficiency curve obtained from the simulation.

It is expected that the calculated addback efficiency in the close geometry of the present setup and in the presence of complicated cascades will show a strong dependence on summing effects. The fluctuation in the values of addback efficiency (Fig. 2.9) can be partially explained by the probability to have

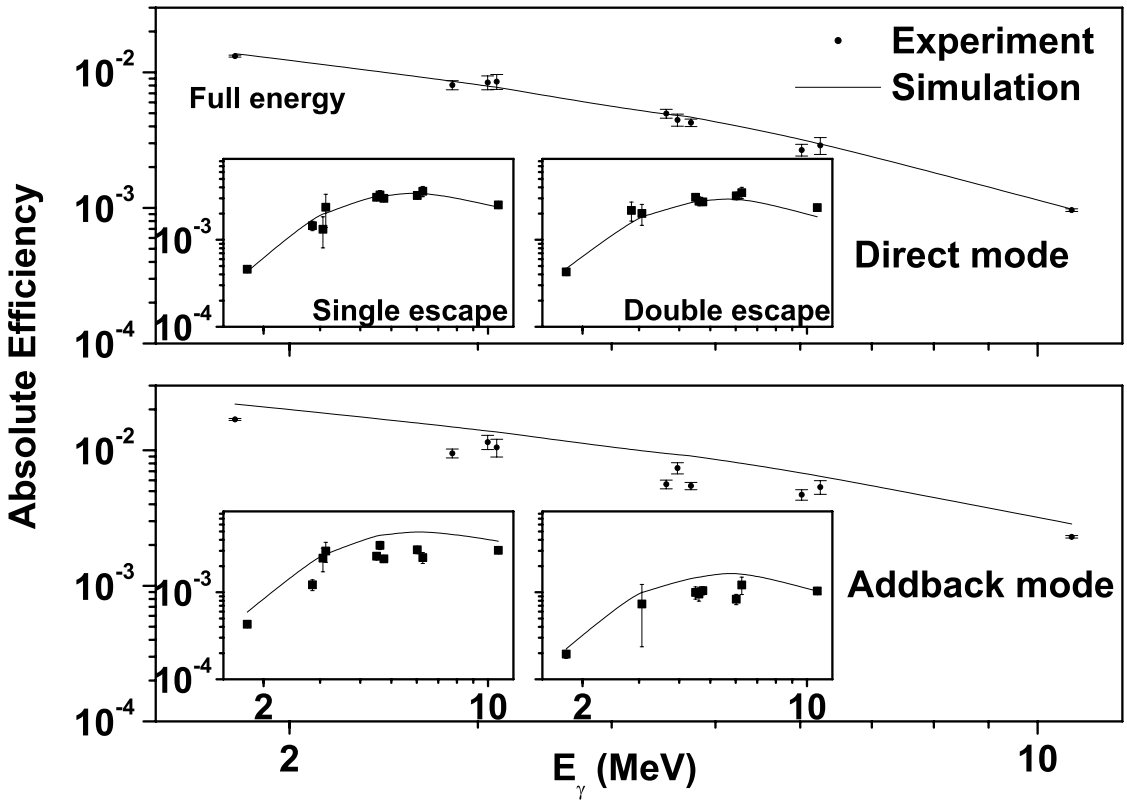


**Figure 2.9: Clover efficiency curves for both addback and direct modes.**

coincidences between the respective transition and the 1779 keV first excited state transition where the detection efficiency is relatively high. For example, if we consider the three transitions of energies around 4.5 MeV, namely 4.497, 4.608 and 4.743 MeV, the probabilities for such coincidences are 100%, 17% and 100%, respectively. These values are calculated from the relative gamma intensities obtained from [NuDat02]. The relatively higher observed addback efficiency for the 4.608 MeV line is consistent with the low probability for the corresponding cascade to pass through the first excited state. Needless to say, coincidences with other cascade gammas do also contribute to the observed summing effect.

It is worth examining this observed fluctuation in the addback detection efficiency in more detail. Depending on the decay scheme, the summing effect for a given $\gamma$-line in the spectrum could yield an increase or decrease in the observed events under the full energy peak [Deb88, Kno00]. Those summing-in and summing-out effects can be investigated using list file event manipulation in LiMDA as described earlier in this chapter (Subsection 2.1.2). For example, by setting a window on the Clover addback spectrum for the energy region corresponding to transitions from the capture state directly to the ground state

(Fig. 2.10a), one can investigate in direct mode the events summing into that region (Fig. 2.10b). Those events include, as expected, Compton scattered photons, escape peaks and annihilation photons which are intended to be collected in addback mode for efficiency enhancement. The above mentioned drawback of the addback mode is illustrated by the full energy peaks clearly identified in Fig. 2.10b which are doubtless cascade transitions summing into the window region. The 1779 keV line is a prominent example.

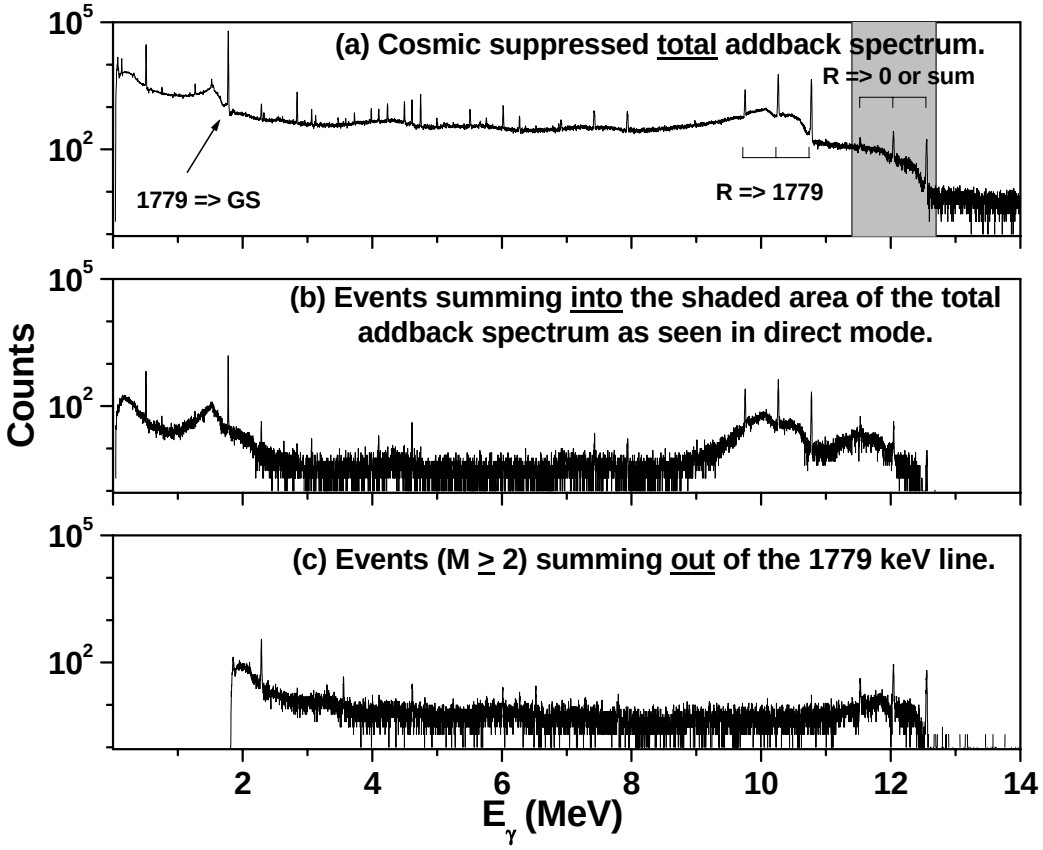


**Figure 2.10: Summing effects in addback mode. Events summing into the R⇒0 energy region are distinguished (in direct mode) by setting a window on the Clover addback spectrum. Events summing out of the 1779 keV line are those of multiplicities ≥2 while setting windows on individual crystal spectra.**

On the other hand, by setting windows on the energy spectra of the individual crystals and inspecting the suppressed events with multiplicities higher than 2, the summing-out effect can be studied. In Fig. 2.10c, the original list mode events have been suppressed by setting windows around the 1779 keV transition from the first excited state to the ground state in every single crystal spectrum. The addback spectrum of the reduced events with multiplicity

higher than 2 corresponds to the losses in the 1779 keV peak due to summing-out effects.

The above example shows qualitatively the summing-in and summing-out contributions to the evident fluctuation in the efficiency calibration curve for the addback mode (Fig. 2.9). The analytical treatment of the correction must, therefore, consider not only the peak efficiencies of the single crystals but also the total efficiencies of the Clover in addback mode. The former information is rather well determined and can be simply inferred from the direct mode efficiency calibration that shows good agreement between experiment and monoenergetic simulation. On the other hand, obtaining the total efficiencies is not straightforward and requires more detailed considerations.

For the experimental determination of the total efficiencies, single-line photon emmiters are definitely best suited [Deb88]. Practically, this is not possible in the energy region under consideration. As an alternative, Monte Carlo simulations have been performed, which solve the problem of monoenergetic photons of energy up to 11 MeV and the effect of the surrounding material, especially of the lead shield, on the total efficiencies as well. Fig. 2.11 depicts the results of the simulation. Obviously, the total efficiencies depend sharply on the geometry of the setup, in the present case particularly on the effect of the lead shield. This implies a fairly complex behaviour of the addback photopeak efficiency.

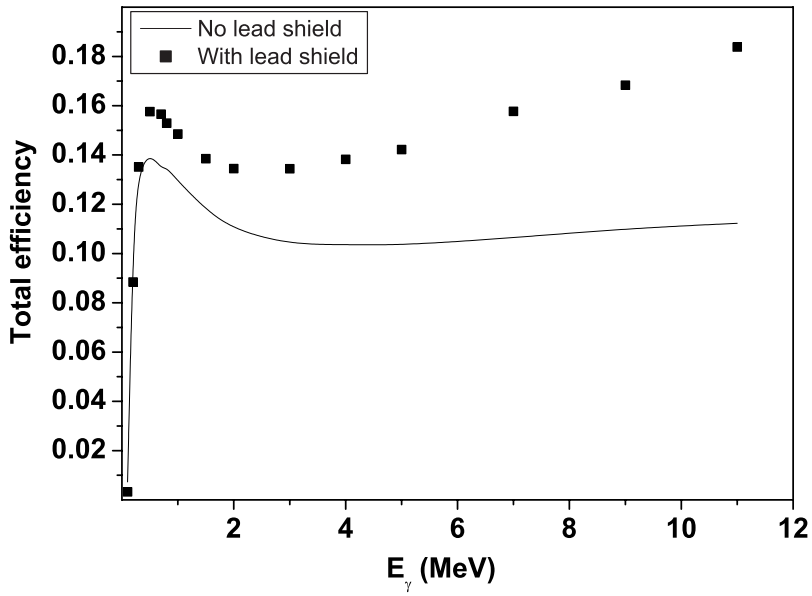


**Figure 2.11: Total efficiency in addback mode for monoenergetic photons obtained from Geant4 simulations, illustrating the large effect of scattering and annihilation photons from the surrounding lead shield.**

As a conclusion, addback calculations are useful to qualitatively examine spectra where weak features are more likely to be distinguished when compared to direct mode. When summing effects from $\gamma$-ray cascades are expected and quantitatively reliable analyses are needed, direct mode data should always be retained. The consequences for the present analysis will be that direct mode data will be adopted for studying the reference resonances at high energies, where BGO coincidences are not required. For the more critical situation with the low energy resonances, where background suppression by BGO coincidences becomes important, the corresponding use of the addback mode of operation still needs to be discussed in detail (Subsection 3.2.2).

The effect of angular distribution on the calculated efficiency values has been also investigated. All the transitions used in the present efficiency measurement are nearly isotropic without high and confusing $\alpha_4$ terms. The $2^{nd}+4^{th}$ order terms: $\alpha_2 P_2(\cos\theta)$ + $\alpha_4 P_4(\cos\theta)$ have been calculated where the $\alpha$-values have been taken from [Ant77]. The angular distribution correction factor for each $\gamma$-transition has been estimated for the present setup and found to have insignificant effect on the calculated efficiencies.

The above discussion about efficiencies serves mainly to investigate the quality of addback calculations when cascade transitions are considered. The method used to finally determine the strengths of the low-energy, weak resonances in the $^{18}$O($\alpha$,$\gamma$)$^{22}$Ne reaction, will be discussed in Chapters 3 and 4. It relies on comparisons of characteristic features observed for the low energy resonances and of reference resonances at higher energies. The efficiencies deduced in this chapter will be used to study those reference resonances.

### 2.3.3 Doppler correction

When a $\gamma$-ray is emitted by a nucleus which is moving with respect to the detector, an energy shift is observed. This is the Doppler effect. Combined with the recoil effect, which is implied by conservation of momentum, an observed $\gamma$-ray energy is then given by

$$E_\gamma = \left(E - \frac{E^2}{2Mc^2}\right)\left(1 + \frac{v}{c}cos\theta\right), \tag{2.3}$$

where $E$ is the transition energy, $M$ is the mass of the nucleus, $v$ is its velocity before $\gamma$-ray emission and $\theta$ is the emission angle with respect to $v$. Since the direction of $v$ for capture reactions is the direction of the incident beam, the maximum observed energy is in the forward direction and the minimum is at backward angles. While theoretically a sharp $\gamma$-ray line is observed at each angle, the observed width is determined by the finite extension of the detector solid angle.

The granularity of the Clover detector helps to correct for the broadening resulting from the large solid angle which strongly reduces the resolution of

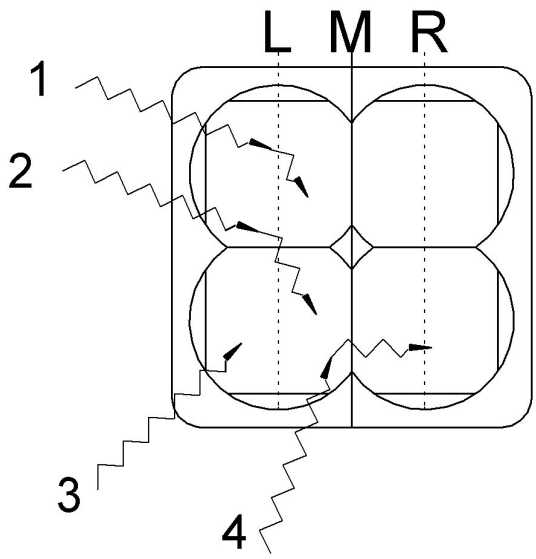


**Figure 2.12: Left "L" and right "R" halves of the Clover as defined for Doppler correction. Events in any half are either of single or double multiplicities (events 1,2 & 3 in the left half). Events in the middle "M" are of double multiplicity corresponding to a $\gamma$-ray scattering between the two halves of the Clover array (event 4).**

such a large detector. This can be achieved by looking at the Clover as being composed of two halves each consisting of two crystals. The left and right halves are separated by the vertical symmetry axis passing through the center (Fig. 2.12). Whenever a $\gamma$-ray hits one crystal (multiplicity 1) or scatters between the two crystals of the same half (multiplicity 2), its angular position is taken for Doppler correction as that which corresponds to the center of that half. This defines two angular positions, "L" and "R" in Fig. 2.12. Events 1,2 and 3 in the figure thus belong to the left half "L".

The third angular position "M" is defined by the position of the vertical symmetry axis of the Clover which separates the two halves. For the full-energy peak events resulting from the coincidence between two adjacent Clover crystals, more than 75% of the events correspond to Compton scattering with the first interaction point located within 20 mm around the surface separating the crystals [Duc99]. Therefore, if a $\gamma$-ray scatters between the two Clover halves (event 4 in Fig. 2.12), it yields a double multiplicity event which corresponds to angular position "M" in the figure.

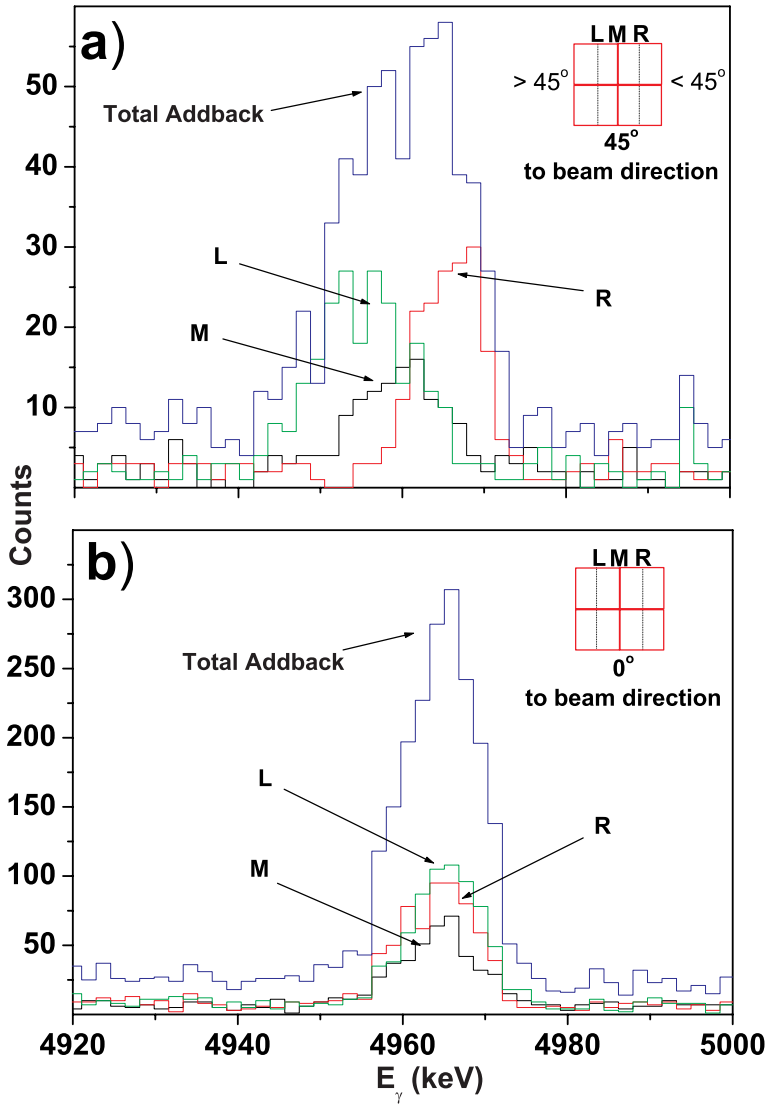


**Figure 2.13: Doppler shift illustrated by the transition from the resonant state to the 5.326 MeV state in the $^{18}$O($\alpha$,$\gamma$)$^{22}$Ne reaction (750 keV resonance). a) For a measurement with the Clover axis at 45$^{o}$ to the beam direction illustrating the different energy shifts on both halves of the Clover. b) For the standard setup (Fig. 2.1) at 0$^{o}$ where symmetry around this angle results in equal shifts seen on both halves. The "L", "M" and "R" detection positions as well as the corresponding multiplicities are defined in Fig. 2.12 and explained also in the text.**

This method has been tested using the 750 keV resonance of the $^{18}$O($\alpha$,$\gamma$)$^{22}$Ne reaction, both for the standard setup with the Clover axis positioned at 0$^{o}$ to the

beam direction (Fig. 2.1) and for another position at 45°. The transition from the resonant state to the 5.326 MeV state has been measured in both cases (Fig. 2.13a&b). The Doppler broadening resulting from the different detection angles of the two halves is clear in Fig. 2.13a. In the final measurement of the $^{18}O(\alpha,\gamma)^{22}Ne$ reaction, the Clover has therefore been placed at 0° to the beam direction where Doppler broadening is minimum (Fig. 2.13b).

## 2.4 Target preparation and stability

The $^{18}O$ targets have been prepared at the Institut für Materialforschung I, Forschungszentrum Karlsruhe. $Al_2{}^{18}O_3$ films have been deposited onto 0.4 mm thick Ta backings by reactive sputtering in an $Ar/{}^{18}O_2$ mixture at 0.4 Pa. The $^{18}O_2$ gas was of high purity, >99.9% in chemical composition and 96.6% in isotopic content, and an aluminium disk of high purity (99.999%) has been used as the sputtering cathode. The same method has been used to prepare natural oxygen $Al_2O_3$ layers for background measurements.

The search for low energy resonances has been performed using 95 $\mu g/cm^2$ $Al_2{}^{18}O_3$ films. Thinner $^{18}O$ targets ($\sim$ 35 $\mu g/cm^2$) have been used to study the high energy resonances at $E_\alpha$ = 750 and 770 keV.

The target stoichiometry has been investigated using the 992 keV resonance of the $^{27}Al(p,\gamma)^{28}Si$ reaction. The measurement was carried out by comparing the yield from pure Al and $Al_2O_3$ targets. The thick target yield (Eq. 2.1) of a resonant reaction is influenced by the rate at which the incident charged particle loses energy in traversing the target [Rol88]. The target to be tested ($Al_2O_3$) consists of a chemical compound containing active (in this case $^{27}Al$) and inactive ($^{18}O$) atoms, thus the resonant thick target yield is reduced by the amount by which the inert atoms participate in the slowing down process of the projectiles [Gov60, Rol88]:

$$T(E)_{eff} = T(E)_{^{27}Al} + \frac{N_{^{18}O}}{N_{^{27}Al}} T(E)_{^{18}O} \tag{2.4}$$

where $N_{^{27}Al}$ and $N_{^{18}O}$ are the number of active and inert atoms in the compound, respectively. By using Eqs. 2.1 and 2.4 as well as proton stopping power values in aluminium and oxygen from [SRIM00], the calculated yield ratio from both targets, assuming $Al_2O_3$ stoichiometry for the compound, is $Y_{Al}/Y_{Al_2O_3} = 2.12$. This ratio is in good agreement with the experimental value of $2.18 \pm 0.04$.

Target stability is a critical concern in a measurement where the low reaction yield implies the need for long runs with high beam currents on target. The stability has been checked and was found to be excellent up to 14 C for an alpha beam of $\sim$120 $\mu$A on target. Fig. 2.14 shows a profile of the $^{18}O$ content

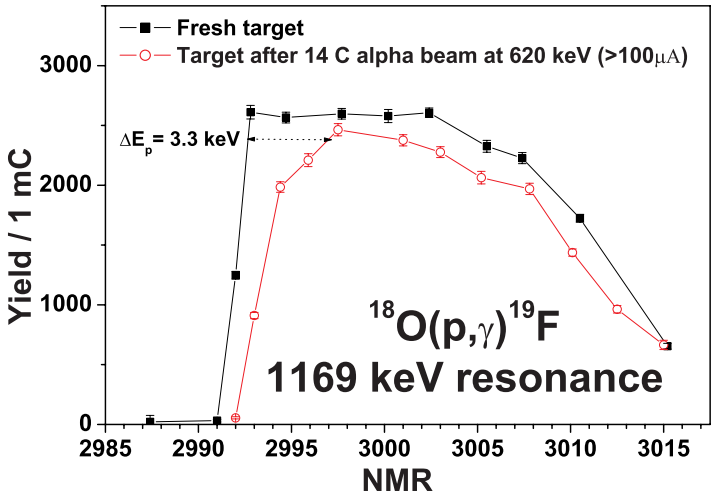


**Figure 2.14: Target stability test using the yield obtained for the 1169 keV resonance of the $^{18}O(p,\gamma)^{19}F$ reaction vs. the magnetic field of the analyzing magnet. Also indicated is the surface damage region of 3.3 keV proton energy width which is equivalent to 21 keV for alpha beam at 600 keV.**

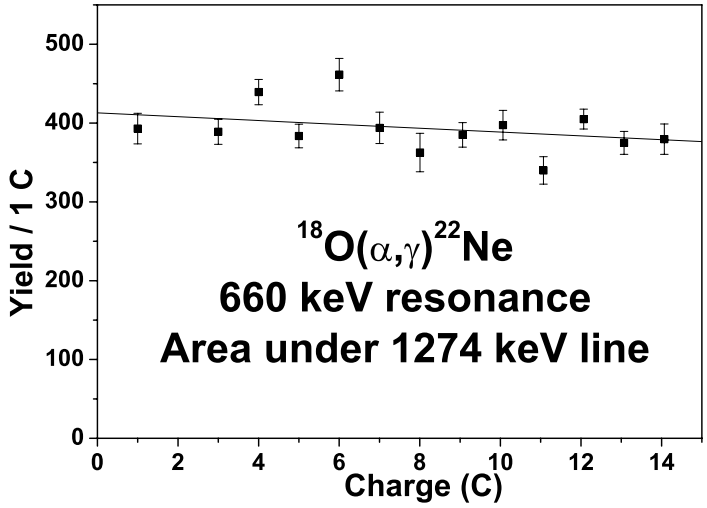


**Figure 2.15: Verification of the target stability using the 660 keV resonance of the $^{18}O(\alpha,\gamma)^{22}Ne$ reaction. The beam energy was kept well above the resonance energy to avoid the surface damage region.**

in a fresh target and in a target which was exposed to a total of 14 C in a measurement of the low energy resonance. The profile has been made using the 1169 keV resonance of the $^{18}O(p,\gamma)^{19}F$ reaction. It shows the effect of surface damage presumably due to a change in stoichiometry by beam interaction with

the $Al_2O_3$ layer. Nevertheless, the profile plateau scanned with protons is well stable bearing in mind the longer width of this plateau for an alpha particle beam. The surface damage region of $\Delta E_p$<3.3 keV indicated in the figure is equivalent to 21 keV for an alpha beam at 600 keV, a result obtained from SRIM2000 simulations [SRIM00]. The corresponding region of surface damage has been accounted for during the search for low energy resonances by keeping the alpha energy well above the expected resonance position. Due to this surface damage, the thinner targets mentioned above show much faster deterioration. In this context it was important that the beam was homogeneously wobbled across the target.

The target stability has also been verified during the experiments by investigating the yield from the 660 keV resonance of the $^{18}O(\alpha,\gamma)^{22}Ne$ reaction in steps of 1 C up to a total integrated charge of 14 C. The performance of a thick target is shown in Fig. 2.15.

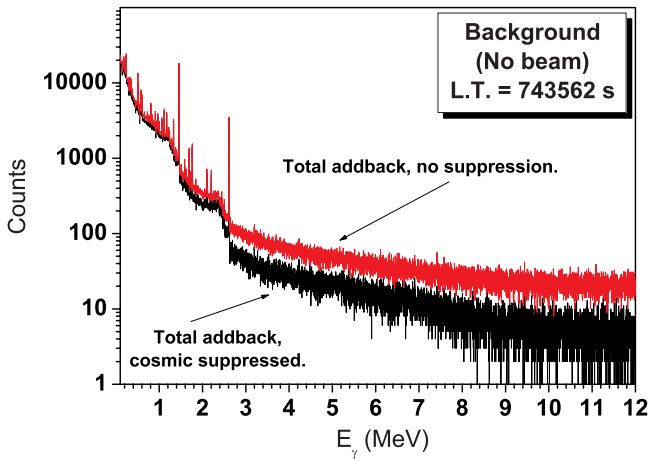


**Figure 2.16: Suppression of the secondary cosmic-ray component in the background spectrum using the plastic scintillator panels on top of the setup (Fig. 2.1).**

## 2.5 Secondary cosmic ray suppression

Background spectra, with and without beam, have been acquired. Background with beam measurements were performed with $\alpha$-particle beams of 620 and 530 keV energy on natural $Al_2O_3$ targets. Apart from the natural room background ($^{40}K$, $^{208}Tl$, etc...) and the $^{214}Bi$ lines from the passive lead shield, additional background components have been identified. In the high energy region, the 6.13 MeV $\gamma$-line from the $^{19}F(p,\alpha\gamma)^{16}O$ reaction induced by a residual proton

component in the alpha beam hitting the magnet wall has been identified. Also clear in the Ge background spectra is $^{207}$Bi pollution found in the BGO scintillation material. $^{207}$Bi does not form part of any natural decay chain. It is likely to be produced by cosmic proton bombardment of $^{206}$Pb [Lew88] or due to atmospheric nuclear weapon tests [Jun01]. $^{60}$Co lines from neighboring magnets in the experimental area have been identified as well.

Possible contribution from these background components to the coincidence spectra acquired for the low energy resonances in the $^{18}$O($\alpha$,$\gamma$)$^{22}$Ne reaction has been investigated, but no background lines could be identified.

Fig. 2.16 illustrates the suppression of the secondary cosmic-ray induced background by means of the plastic scintillator sheets on top of the experimental setup (Fig. 2.1). The corresponding suppression factor has been found to be 2.6 in the $\gamma$-energy region 3-11 MeV and 3.4 in the energy region 7-11 MeV.

## 2.6 Experimental runs

After several test measurements, the setup has been finally optimized as described in Fig. 2.1 and throughout this chapter. Table 2.2 provides an overview of the experimental runs in the measurement of the low energy resonances as well as the known reference resonances in the $^{18}$O($\alpha$,$\gamma$)$^{22}$Ne reaction.

The excitation function of the reference resonances have been scanned to check the energy calibration of the accelerator as well as to choose the proper energy values for long runs intended to analyze the decay schemes of these resonances. The detailed procedures and results are given in Chapter 3. Finally, the weak low-energy resonances have been measured in long runs with different $\alpha$-beam energies on the plateau of the thick target excitation function. The background contribution of the beam has been tested using natural oxygen targets (Section 2.4).

**Table 2.2: Different experimental runs in search of the low energy resonances as well as those of the reference resonances in the $^{18}$O($\alpha$,$\gamma$)$^{22}$Ne reaction. Runs on natural oxygen targets were used to examine the background contribution. The listed values for the beam current and target thickness are representative.**

| $E_\alpha$ (keV) | Beam current ($\mu A$) | Charge ($C$) | Target | Resonances (keV) |
|---|---|---|---|---|
| 780 | 120 | 4 | $^{18}$O, $\Delta E$= 45 keV | 750 and 770 |
| 765 | 120 | 5 | $^{18}$O, $\Delta E$= 45 keV | 750 |
| 700 | 100 | 14 | $^{18}$O, $\Delta E$= 125 keV | 660 |
| 650 | 100 | 10 | $^{18}$O, $\Delta E$= 90 keV | 566 |
| 640 | 100 | 35.5 | $^{18}$O, $\Delta E$=125 keV | 566 |
| 620 | 100 | 27 | $^{18}$O, $\Delta E$=123 keV | 566 |
| 600 | 100 | 25 | $^{18}$O, $\Delta E$=123 keV | 566 |
| 530 | 50 | 6 | $^{18}$O, $\Delta E$=120 keV | 470 |
| 520 | 50 | 27.3 | $^{18}$O, $\Delta E$=120 keV | 470 |
| 620 | 100 | 31 | Natural oxygen, $\Delta E$=123 keV | Background |
| 520 | 50 | 8 | Natural oxygen, $\Delta E$=120 keV | Background |

# Chapter 3

# MEASUREMENT OF THE REFERENCE RESONANCES

The present experimental investigation of the $^{18}O(\alpha,\gamma)^{22}Ne$ reaction below 800 keV is given in this and the following chapters. To start with, the reference resonances at 600, 750, and 770 keV are studied in detail for understanding the possible decay modes as well as for determining the corresponding branching ratios. The different coincidence techniques required for investigating the much weaker resonances at astrophysical energies are discussed and applied to the reference resonances. This sets the ground for the study of the low energy resonances that will follow in Chapter 4. Finally, the astrophysical implications of the combined results are discussed in Chapter 5.

## 3.1 Decay modes

Although the resonances of the $^{18}O(\alpha,\gamma)^{22}Ne$ reaction at $E_a$ = 660, 750 and 770 keV have been previously described [Tra78, Vog90, Gie94], the decay schemes of these resonances have never been reported in detail. The available information regarding the parameters of these resonances are summarized in Table 3.1. Since the determination of the strengths of the low energy resonances is to be based on the coincidences between the measurement of the secondary transition ($1^{st}$ excited state $\rightarrow$ ground state) detected in the Clover and the primary transitions detected in the BGO's, information on the decay scheme is crucial for this work. In particular, it is necessary to determine the fraction of the total decays passing through the first excited state at 1274 keV and that bypassing it.

The study of the spectra at these resonances reveals new details about the decay modes and branching ratios. Figures 3.1, 3.2 and 3.3 show primary transitions for all three resonances. The rather complicated spectrum of Fig. 3.3 includes the features of both resonances at 750 and 770 keV. The asterisks

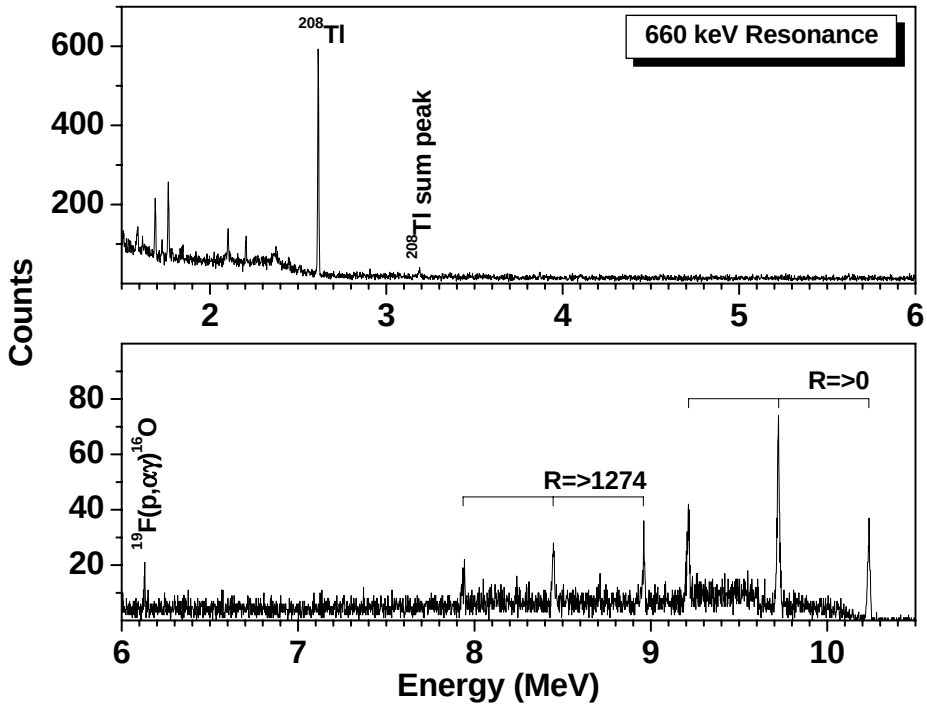


**Figure 3.1: Cosmic suppressed spectrum acquired for the 660 keV resonance using a thick target and an integrated beam current of 14 C.**

**Table 3.1: Parameters of the reference resonances in the $^{18}$O($\alpha$,$\gamma$)$^{22}$Ne reaction available from the literature.**

| $E_R$ (keV) [a] | $E_x$ (keV)[a] | $J^\pi$ [b] | $\omega\gamma$ ($\mu eV$) |
|---|---|---|---|
| 662.1 $\pm$1.0 | 10211.0 | $1^-$ | 212 $\pm$42[b] |
| | | | 290 $\pm$50[c] |
| | | | 230$\pm$25[a] |
| 749.9 $\pm$1.0 | 10282.7 | $0^+$ | 560$\pm$60[a] |
| 767.6 $\pm$1.0 | 10297.3 | $2^+$ | 1200$\pm$120[a] |

[a] Ref. [Vog90]
[b] Ref. [Gie94]
[c] Ref. [Tra78]

indicate transitions which receive contribution from both resonant states. The excitation function for these two resonances is shown in Fig. 3.4.

All spectra have been carefully analyzed. Due to the relatively short lifetime of the thin targets used for the 750 and 770 keV resonances, and the need to

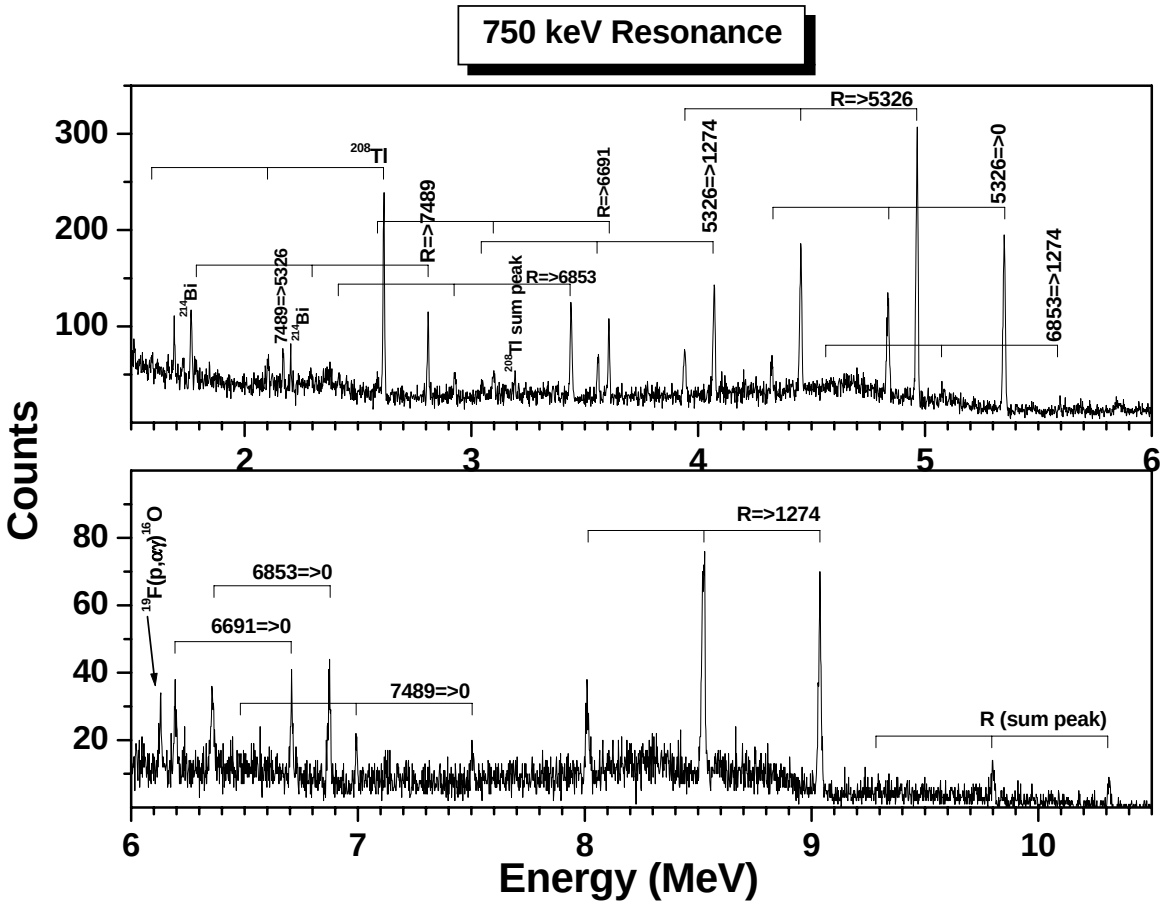


**Figure 3.2: Cosmic suppressed spectrum acquired for the 750 keV resonance using a thin target and an integrated beam current of 4.88 C.**

acquire good statistics, the spectra measured in long runs have been corrected for target deterioration. This was achieved by comparing the 1274 keV yield from the long run to that of a fresh target measured at the same α-energy with only 1 C. The corrected charge for both long runs, namely for the 750 keV resonance alone and for the 750 and 770 keV resonances together, has been found to be 4.9 and 3.3 C, respectively. To obtain the net yield from the 770 keV resonance, the first spectrum has been subtracted from the second after normalization. Two examples are given in Fig. 3.5, where primary transitions to three bound states are illustrated.

The identified primary transitions as well as the corresponding branching ratios are summarized in Table 3.2. The results from both direct and addback mode calculations are listed for comparison. Though the yield for the full energy peak is smaller in direct mode than in addback mode, the results

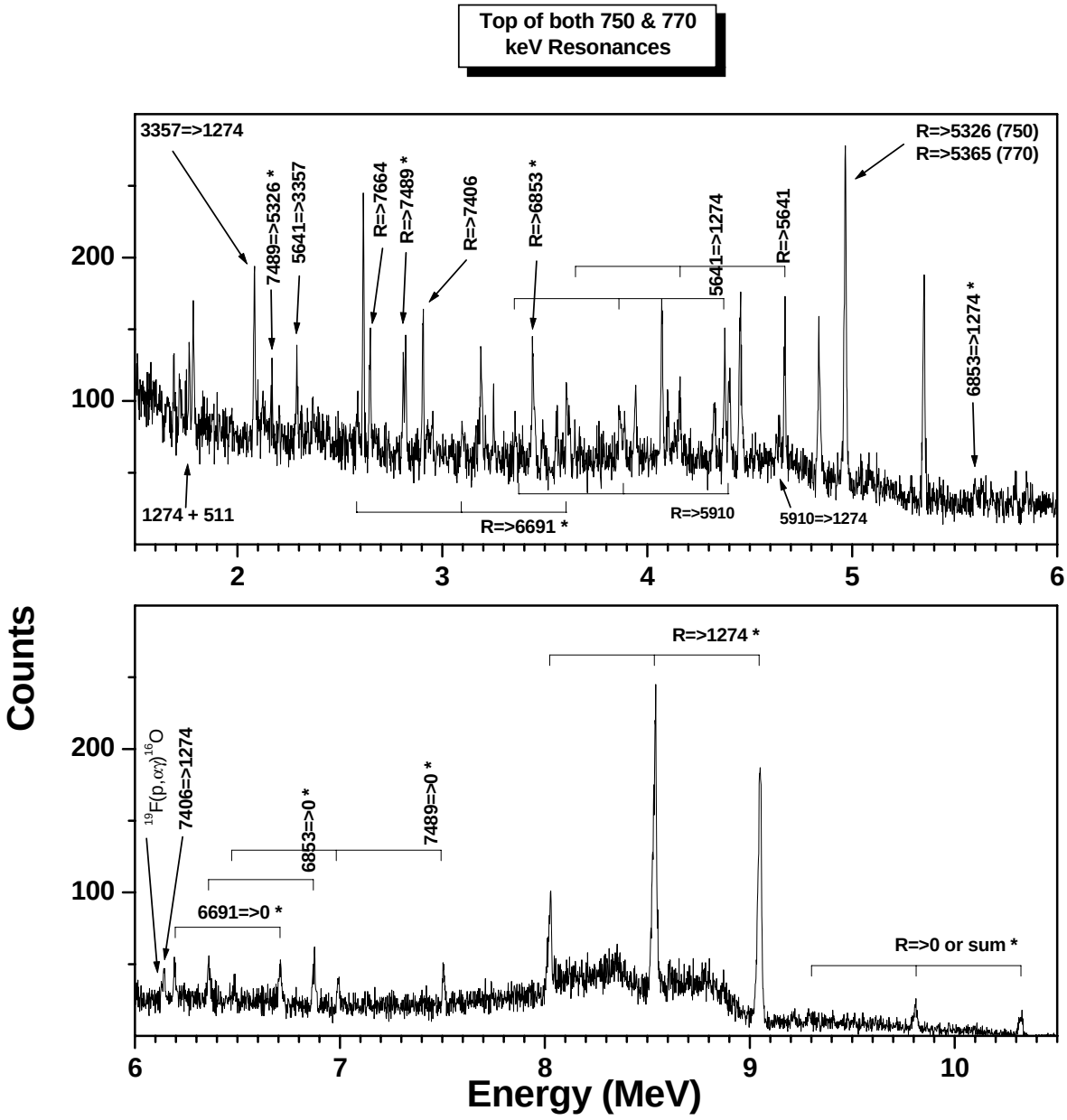


**Figure 3.3: Cosmic suppressed spectrum acquired for the 750 and 770 keV resonances using a thin target and an integrated beam current of 3.3 C. The asterisks indicate transitions that receive contributions from both resonant states. The unmarked transitions belong to the 750 keV resonance only and are identified in Fig. 3.2.**

**Table 3.2: Branching ratios obtained in this work for the three reference resonances. The results from the analysis of cosmic suppressed Clover spectra in direct as well as in addback mode are listed.**

| | Addback | Direct |
|---|---|---|
| 660 keV resonance | | |
| R $\Longrightarrow$ 1274 | 27.8±5.1 | 28.0±6.0 |
| R $\Longrightarrow$ 0 | 72.2±7.0 | 72.0±5.3 |
| 750 keV resonance | | |
| R $\Longrightarrow$ 7489 | 5.5±1.3 | 6.6±1.0 |
| R $\Longrightarrow$ 6853 | 11.5±2.3 | 9.7±1.6 |
| R $\Longrightarrow$ 6691 | 6.6±1.3 | 5.9±1.3 |
| R $\Longrightarrow$ 5326 | 47.3±7.1 | 46.9±4.6 |
| R $\Longrightarrow$ 1274 | 25.4±4.5 | 29.5±4.0 |
| R $\Longrightarrow$ 0 or sum | 3.7±0.7 | 1.4±0.5 |
| 770 keV resonance | | |
| R $\Longrightarrow$ 7664 | 3.5±0.9 | 4.3±0.8 |
| R $\Longrightarrow$ 7489 | 3.2±0.8 | 3.3±0.7 |
| R $\Longrightarrow$ 7406 | 4.8±1.2 | 4.9±0.7 |
| R $\Longrightarrow$ 6853 | 3.0±0.7 | 2.7±0.8 |
| R $\Longrightarrow$ 6691 | 3.9±0.8 | 4.7±0.8 |
| R $\Longrightarrow$ 5910 | 5.7±0.9 | 6.0±0.9 |
| R $\Longrightarrow$ 5641 | 8.1±1.2 | 8.5±1.0 |
| R $\Longrightarrow$ 5365 | 6.4±1.1 | 6.2±0.9 |
| R $\Longrightarrow$ 1274 | 55.0±8.8 | 57.2±5.2 |
| R $\Longrightarrow$ 0 or sum | 6.4±0.8 | 2.2±0.4 |

obtained in direct mode are in general more accurate because of the smaller uncertainties in the $\gamma$-ray efficiency. In addback mode, summing effects result in experimentally larger branching ratios for the transition from the resonant to the ground state which is in fact forbidden for the 750 keV resonance. Therefore, the branching ratios deduced in direct mode have been adopted. These results are shown in Fig. 3.6 along with the corresponding primary transitions for each resonance.

Using the relative $\gamma$-intensities for the bound states [NuDat02], and the branching ratios for the primary transitions listed in Table 3.2, the probability for decays from each resonant state populating the first excited state has been calculated and given in the left column in Fig. 3.6. This information is extremely useful for the coincidence calculations where the resonances studied in this section will provide the reference to determine the resonance strength of the much weaker resonances at lower energies. The above mentioned determination of the bypasses over the first excited state in the decay scheme will

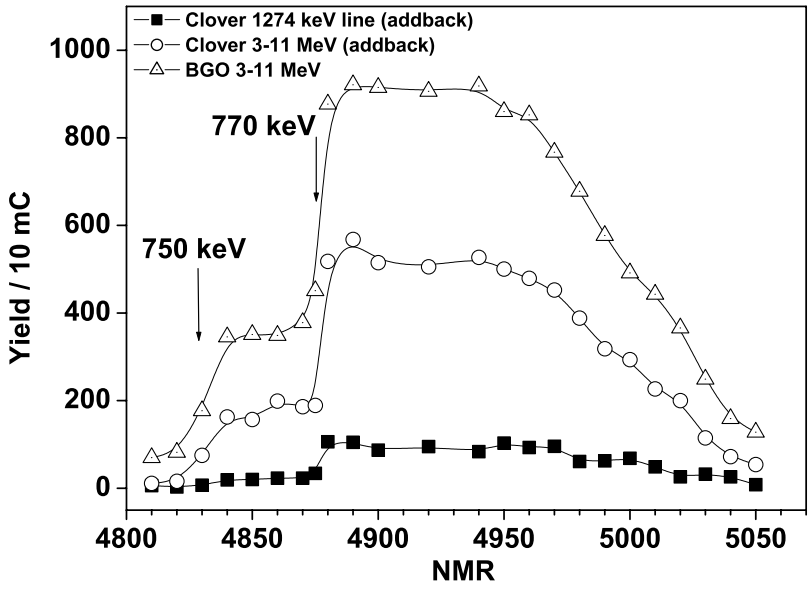


**Figure 3.4: Excitation function of the 750 and 770 keV resonances measured using the Clover detector (1274 keV secondary transition and high energy gammas) as well as the high energy transitions using the BGO detectors.**

provide a correction factor needed in the comparison. The detailed description of the coincidence calculations and the methods used in their analysis will be the focus of the next section.

## 3.2 The coincidence technique

The peak-to-background ratio is the major factor that needs to be optimized in search of extremely weak yields. Since all events are registered in list mode and no online hardware data suppression has been used, off-line data analysis provides a flexible way of testing different possibilities for background reduction. The ultimate goal is to improve the peak-to-background ratio and thus the detection sensitivity. This section starts by outlining the steps leading to the optimal method adopted for the final analysis.

### 3.2.1 Compton suppression vs. coincidences

In an early measurement, the four BGO detectors were placed around the Ge Clover (which was at $45^{o}$ to the beam direction) to test both options, Compton suppression (anticoincidence) and coincidences between cascade transitions. It

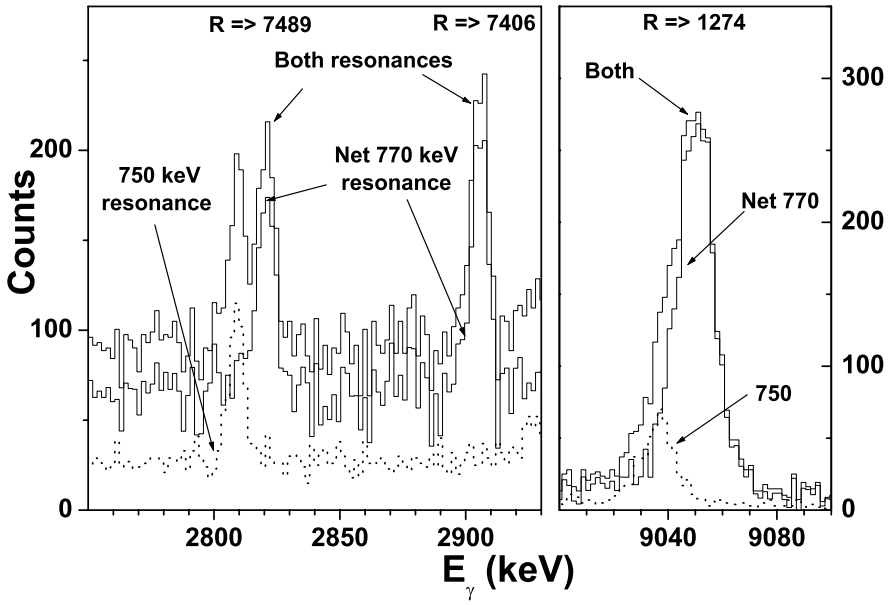


**Figure 3.5: The net contribution of the 770 keV resonance to the total spectrum acquired on top of both 750 and 770 keV resonances as obtained by subtraction of the component due to the resonance at 750 keV.**

was found that the coincidence option using an energy window in the BGO data above 3 MeV provided the best selection. This window includes the primary transitions feeding the first excited state at 1274 keV. This solution leads to an improvement of the peak-to-background ratio by a factor 6.4 compared to the option based on Compton suppression. In spite of the reduction in the number of real counts in case of coincidences, the improved peak-to-background ratio allows to distinguish a clear peak for the 1274 keV line. This comparison facilitated the decision for the final setup (Fig. 2.1) where the BGO detectors could no longer be used for Compton suppression.

Nevertheless, the reduction of Compton background can alternatively be achieved by operating the Clover in addback mode (Section 2.3.1 and Fig. 2.6). Thus, the coincidence spectrum in addback mode would ultimately provide the best peak-to-background ratio.

The main conclusion from that early measurement was to improve counting statistics for coincidences by optimizing the geometry in such a way that the four BGO detectors cover a large solid angle upstream of the target position (Fig. 2.1). Correspondingly, the efficiency for the coincident detection of cascade transitions as defined by the net area under the 1274 keV line could be improved by a factor of two. A detailed quantitative analysis will be given below. In addition, the $0^o$ orientation of the final detection geometry relative to the

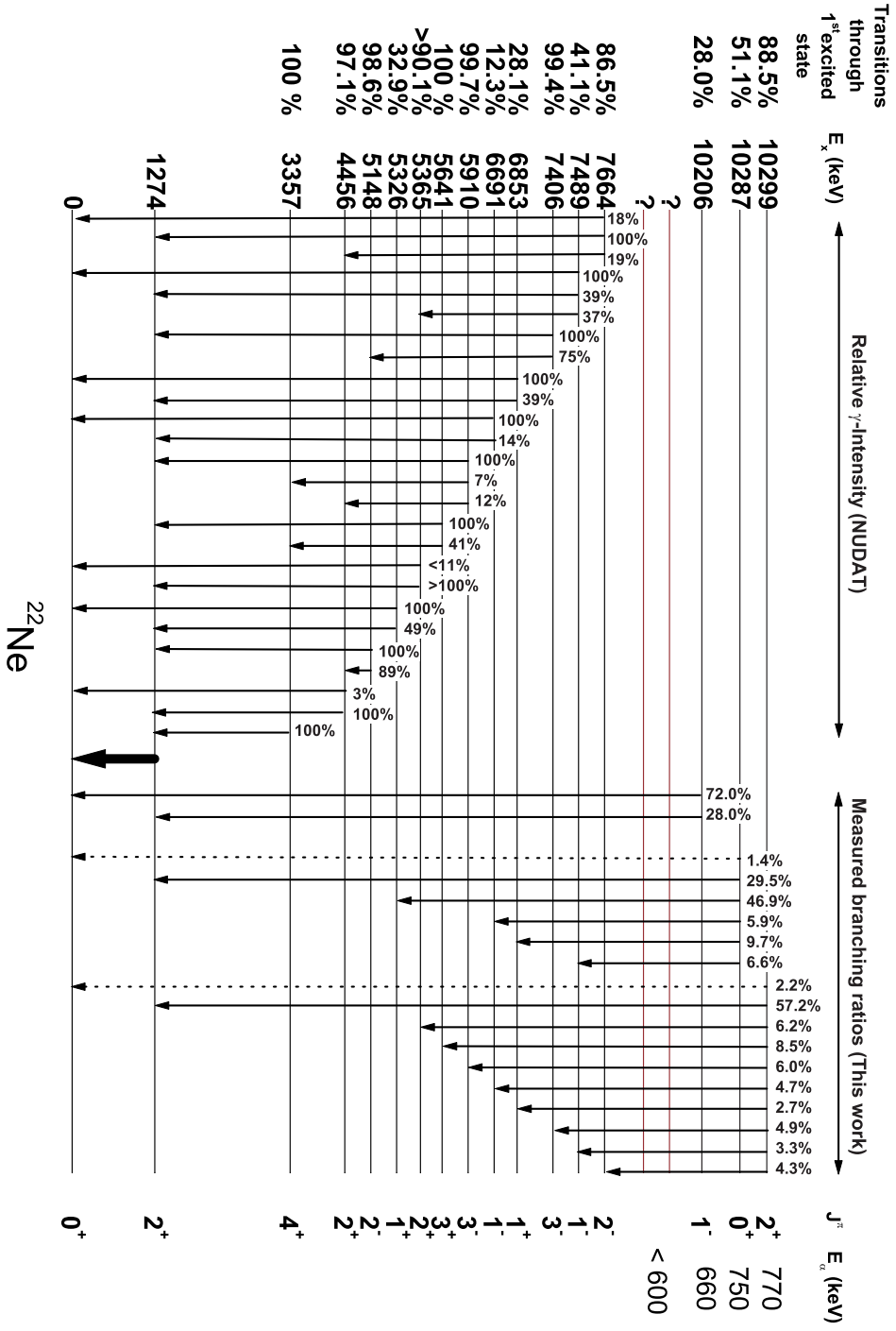


**Figure 3.6: Decay modes identified for the resonances at 660, 750 and 770 keV $\alpha$-energy. The much weaker resonances at lower energies, which are to be studied in Chapter 4, are denoted by question marks.**

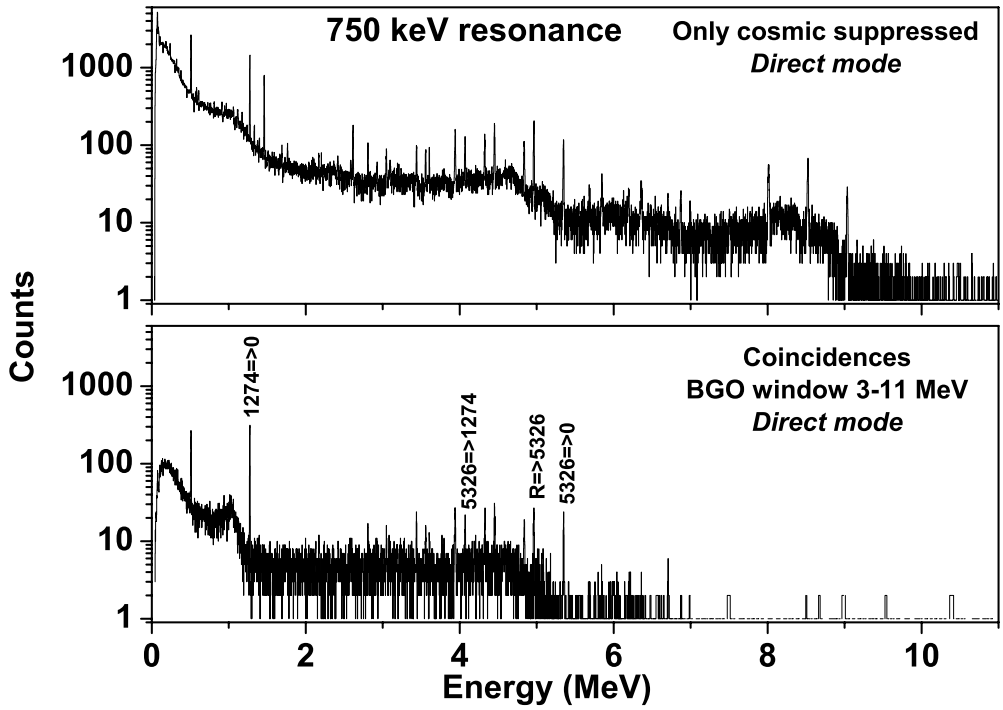


**Figure 3.7: The Ge Clover spectrum taken on the 750 keV resonance with an integrated beam current of 4.88 C. The top panel shows the situation if only the plastic scintillators covering the experimental setup are used for reduction of the secondary cosmic ray background. The bottom panel shows the coincidence spectrum obtained with a BGO window of 3-11 MeV. The improvement in the peak-to-background ratio for the 1274 keV line is obvious.**

beam direction compared to $45^{o}$ used earlier reduces the Doppler broadening of the primary $\gamma$-lines considerably (Section 2.3.3 and Fig. 2.13).

Apart from the BGO energy-window option, the Ge-BGO coincidence spectra can be generated in an alternative way. It considers the whole assembly consisting of the Clover and the BGO's as one calorimeter. A Q-value energy window can then be set and the corresponding Clover data are analyzed only if the total energy deposition in the calorimeter lies within this window. This method imposes additional restrictions on the Clover events since it requires the full energy detection of the cascade photons. The advantage of the BGO energy-window option is that it includes Compton events and not all the cascade photons should necessarily be detected. The experimental observations support this conclusion. The sensitivity for detecting the 1274 keV first excited state transition in the Clover was always superior in the BGO energy-window option to that using the Q-value windows. The best results obtained for the Q-

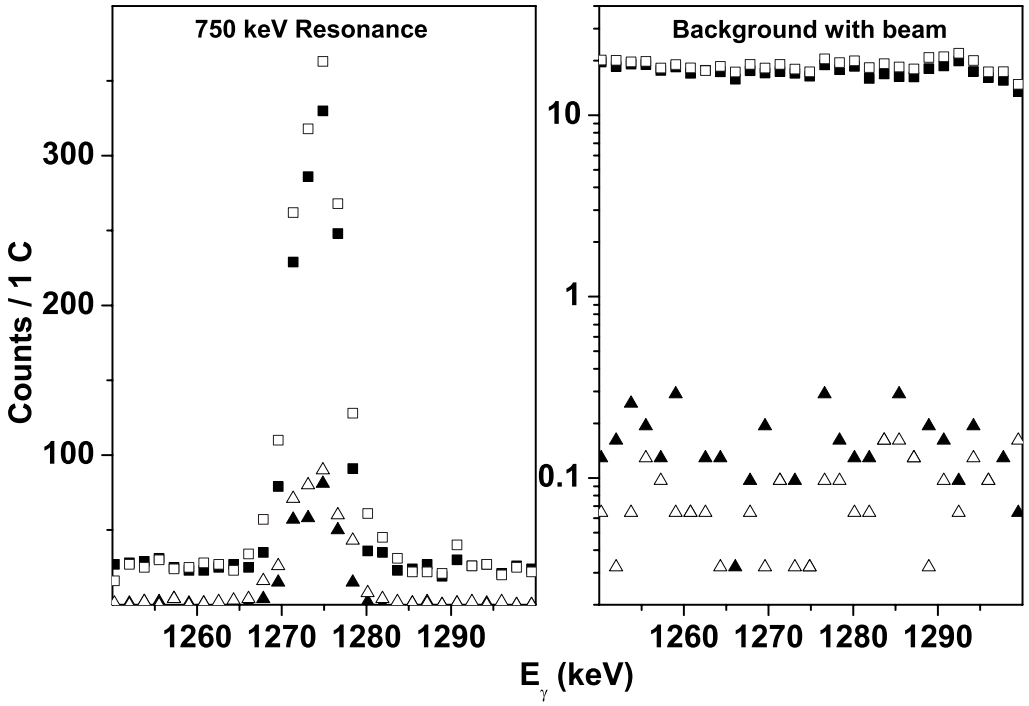


**Figure 3.8: Left panel: Same data as in Fig. 3.7, but zoomed on the 1274 keV transition from the first excited state to the ground state. Right panel: The same energy region is shown for the background run using a natural $Al_2O_3$ target. Both spectra correspond to a collected charge of 1 C. The squares correspond to the spectra in which only the secondary cosmic ray background component is suppressed while the triangles represent the Clover coincidence spectra with a 3-11 MeV window in the BGO data. Closed and open symbols correspond to the direct and addback mode, respectively.**

value option was for the decay of the 660 keV resonance which includes purely two-step cascade.

### 3.2.2 Coincidences and addback mode

With this improvement in the detection sensitivity of coincident cascade transitions, the detection of the 1274 keV line needs to be further optimized. The Clover spectrum recorded in coincidence with the proper energy and time windows in the BGO data (see Subsection 2.1.2), as well as the spectrum for which only the cosmic ray background component is suppressed, are shown in Fig. 3.7 for the 750 keV resonance.

Though the peak efficiency in the coincidence spectrum (bottom panel of

Fig. 3.7) is reduced by a factor 4.4, the corresponding strong background suppression provides a convincing argument in favor of the coincidence option for detecting the much weaker yields anticipated for the low energy resonances. Apart from the 1274 keV transition, several $\gamma$-lines at higher energy, especially from a strong decay mode through the 5326 keV state (see Fig. 3.6) can be identified as well.

The gain in the peak-to-background ratio is shown in more detail in Fig. 3.8 for the energy region around the 1274 keV line. While the yield is lower by a factor 4.4 in direct mode and 3.7 in addback mode (left panel), the background is reduced by factors of 125 and 260 for the coincidence option, in direct and addback mode, respectively (right panel). These ratios suggest that addback, while not required for the high energy resonances where the statistics in direct mode are sufficient, may still be helpful in case of the much weaker low energy resonances. As discussed earlier, the addback mode suffers from uncertainties due to summing effects. However, these effects are strongly reduced in the coincidence spectra. As implied by the geometry of the detection system, the coincidence spectrum includes selectively and by definition those transitions in the cascade that correspond to $\gamma$-photons emitted in opposite directions. That holds in particular for two step cascades which contribute 100%, 30% and 58% to the total decays feeding the 1274 keV level, for the resonances at 660, 750 and 770 keV, respectively (Fig. 3.6).

In order to verify the reduction of the summing effects in the coincidence option, the addback addition factor $f$ defined by

$$f = \frac{N_{addback}}{N_{direct}} - 1 \tag{3.1}$$

(where $N$ is the net number of counts under the 1274 keV line) has been calculated for the spectra in which only the cosmic ray background component is suppressed as well as for the coincidence spectra. For the former case, the addition factor has been found to be 0.32, 0.18 and 0.27 for the three resonances at 660, 750 and 770 keV, respectively. Since the summing effects are expected to be reduced in the coincidence spectra, the addback addition factor should be higher. For the three resonances mentioned above, this factor is 0.58, 0.43 and 0.50, respectively.

According to these considerations, the addback mode will be used when coincidence spectra of the weak resonances are analyzed.

### 3.2.3 Feeding of the first excited state

The analysis of the coincidence spectra of the weak low-energy resonances can be normalized to that of the three higher resonances in order to estimate the strength of the low energy resonances. This procedure must account, however,

for the different decay schemes of the resonances which may result in different feeding probabilities of the first excited state (Fig.3.6). Accordingly, the strength of a weak resonance can be expressed as

$$\omega\gamma\left(E_x\right) = \frac{E_X Y\left(E_X\right) T\left(E_X\right) Q_R}{E_R Y\left(E_R\right) T\left(E_R\right) Q_X} \omega\gamma\left(E_R\right) \left\{\frac{B_R}{B_X}\right\}, \tag{3.2}$$

where "$X$" refers to the unknown (low energy) and "$R$" to the reference (higher energy) resonances, $T$ is the stopping power of α-particles in the $Al_2{}^{18}O_3$ target at the given energy, $Q$ is the total collected charge and $Y$ is the net area under the 1274 keV line in the generated coincidence spectrum. The feeding probability "$B$" of the first excited state has been introduced to correct for possible differences in populating this state. These corrections for the low energy resonances have been estimated as follows:

The different decay modes of any resonance in this reaction can be classified as in the inset of Fig. 3.9. The above mentioned calculation considers modes 1 & 2, and the bypass correction is intended to account for the contribution of the other two modes in the calculation of the resonance strength. Table 3.3 lists the fractional contribution of the four modes to the total decays for each of the three higher energy resonances. The values have been calculated using data from Table 3.2 and Fig. 3.6. It would be necessary to consider mode 3 in the coincidence option in order to correct for the above mentioned bypasses over the first excited state. Obviously, mode 4 can not be accounted for in this respect since the decay goes directly from the resonant state to the ground state. However, this mode is expected to contribute to the total yield only in the decay of the 660 keV resonance ($J^\pi = 1^-$). The calculated resonance to ground state branchings for the 750 and 770 keV resonances (Tables 3.2, 3.3 & Fig. 3.6) could be attributed to summing effects which are larger in addback mode than in direct mode. This was one reason why the direct mode results have been adopted in that particular case.

**Table 3.3: Fractional contribution of different decay modes to the total decays for the high energy resonances (in %).**

| Resonance Energy (keV) | Mode 1 | Mode 2 | Mode 3 | Mode 4 |
|---|---|---|---|---|
| 660 | 28.0±6.0 | 0 | 0 | 72.0±5.3 |
| 750 | 29.5±4.0 | 21.6±1.6 | 47.5±3.6 | 1.4±0.5 |
| 770 | 57.2±5.2 | 31.3±1.9 | 9.3±1.0 | 2.2±0.4 |

The rather important contribution of decay mode 3 has been obtained for the three high energy resonances, as mentioned above, using the singles spectra. Obviously, this method is not expected to be valid in case of the weak yield anticipated for the low energy resonances where no distinguished γ-lines can be measured. In order to investigate the relative contribution of this decay

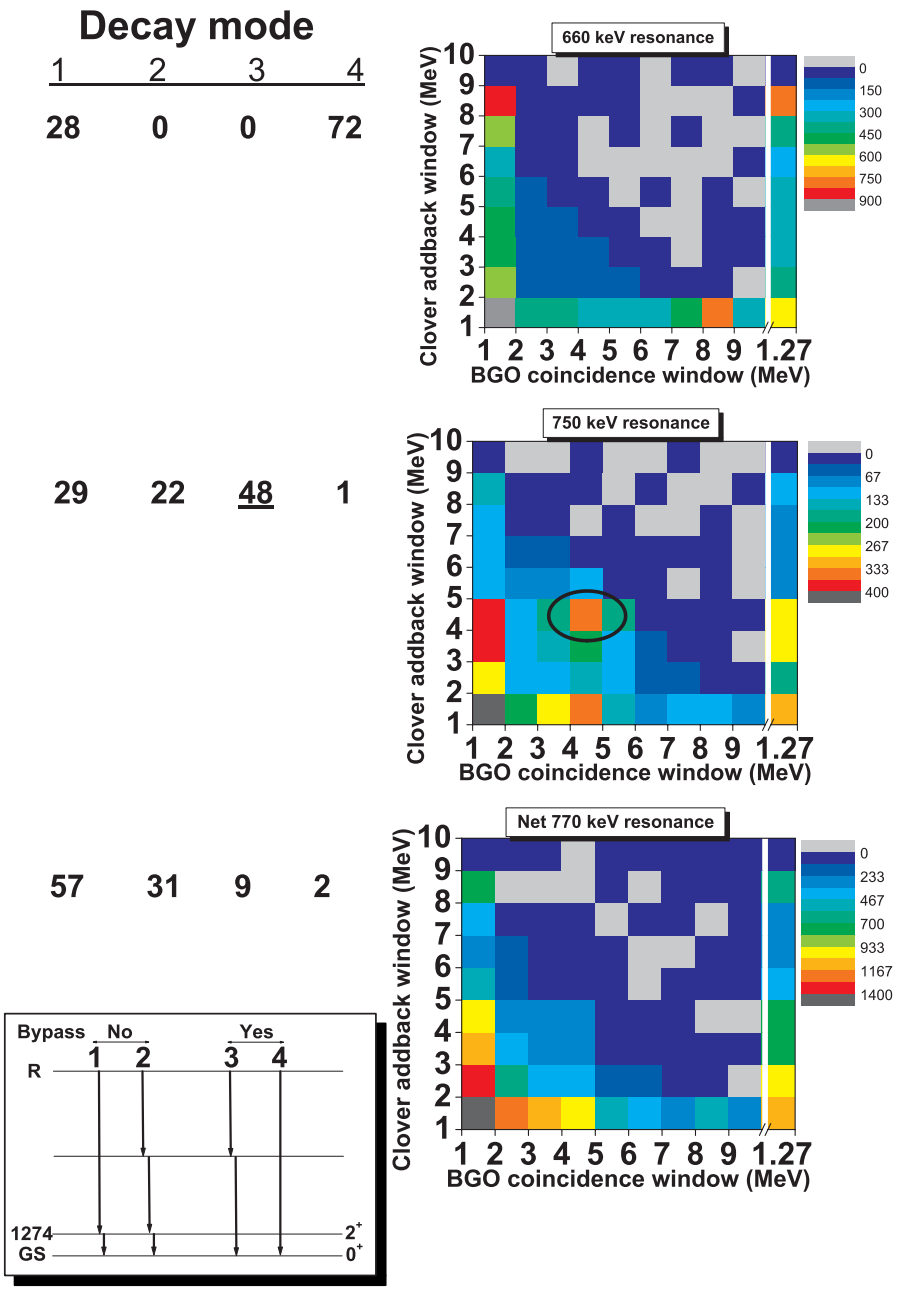


**Figure 3.9: Matrix spectra calculated for the three high energy resonances. A clear "peak" in the 3-6 MeV region (both Clover and BGO) for the 750 keV resonance is consistent with the strong mode 3 transitions for this resonance. The right-most column represents coincidences in a BGO window around the 1274 keV line.**

mode in a different way, three dimensional coincidence 'matrix' spectra have been calculated for each resonance. These matrices (Fig. 3.9) give the number

**Table 3.4: Net area under the 1274 keV line in coincidence with a 3-11 MeV BGO window and the calculated strengths (corrected for bypass over the first excited state) for the 750 and 770 keV resonances relative to that of the 660 keV resonance. The values in brackets are taken from Table 3.1 for comparison.**

| Resonance energy (keV) | Window in any single BGO output | Window in BGO energy sum (BGO addback) | Resonance strength $\omega\gamma$ ($\mu eV$) |
|---|---|---|---|
| 660 | 103 ±3 | 104 ±3 | (230±25) |
| 750 | 411 ±20 | 418 ±20 | 569±70 (560±60) |
| 770 | 1658 ±50 | 1711 ±50 | 1354±157 (1200±120) |

of 'net' events in 1 MeV energy regions in the addback Clover spectrum which are in coincidence with 1 MeV energy windows in the BGO data. Since mode 3 decays bypassing over the first excited state are characterized mainly by $\gamma$-lines in the 3-6 MeV energy range (Fig. 3.6), the corresponding 3-MeV $\times$ 3-MeV region in the matrices gives, at least qualitatively, an idea about mode 3 bypasses. It should be noted that mode 2 also could contribute to this region. A 'peak' inside this "square" is clearly seen in the 750 keV resonance matrix which is consistent with the mode 3 bypasses anticipated from its decay scheme (Fig. 3.6 and Table 3.3).

The validity of the "$B$" factor introduced in Eq. 3.2 can be tested by selecting the 660 keV resonance as a reference and calculating the resonance strengths of the 750 and 770 keV resonances relative to it. The net areas under the 1274 keV line in coincidence with a 3-11 MeV BGO window for the three resonances are listed in Table 3.4. The coincidences have been calculated twice, first with windows in each BGO output (coupling 2 detectors) separately and second by using a window in the energy sum (addback) BGO spectrum. Using Eq. 3.2, the resonance strengths have been calculated relative to the 660 keV resonance and are listed in the last column of Table 3.4. In this calculation, "$B$" factors listed in Fig. 3.6 have been used and the first type of BGO coincidence window has been adopted. The results agree well, within the estimated errors, with those in the literature (Table 3.1). This provides confidence in the bypass correction for the coincidence method to be used for determining the strength of the low-energy resonances provided that the "$B$" factor can also be estimated for these cases.

# Chapter 4

# RESONANCES AT STELLAR ENERGIES

In this chapter, the techniques described earlier will be applied to the low energy resonances (< 600 keV) in order to measure their resonance strengths. Additional fine tuning for the coincidence calculation will be presented.

## 4.1 Previous attempts

Trautvetter *et al.* [Tra78] measured the $^{18}$O($\alpha$,$\gamma$)$^{22}$Ne reaction covering the energy range from 0.6 to 2.3 MeV. Their rate includes the contribution of the resonances in this energy range, as well as contributions of the direct capture process, the wings of a broad resonance at 1.53 MeV and results from a previous work [Ada69] that covered the energy range from 2.15 to 3.70 MeV. The compilation by Caughlan and Fowler [CF88] basically adopted the [Tra78] rate but included an estimate for the resonance at 58 keV. The stellar reaction rate is well determined by these experimental data at temperatures $T_9$=0.3-4.3. Below $T_9$=$\sim$0.3, however, the rate was foreseen to be significantly enhanced if additional resonances could be detected at energies below 600 keV [Tra78, Rol88].

In a later study, Giesen *et al.* [Gie94] used the $^{18}$O($^6$Li,d)$^{22}$Ne $\alpha$ transfer reaction to study the level structure of $^{22}$Ne in the excitation range $E_x$=8.5-11.3 MeV in search for $\alpha$-unbound natural parity states. Four states were observed in that experiment at 9.72, 9.85, 10.05 and 10.13 MeV, corresponding to resonances at $E_\alpha$=58, 218, 470 and 566 keV in the $^{18}$O($\alpha$,$\gamma$)$^{22}$Ne reaction. From their angular distribution measurements of the transfer reaction, they obtained information on the possible angular momentum transfer $l$ to the populated states in $^{22}$Ne. Possible spin assignments for these levels were also obtainable since for these natural parity states the spin and parity are determined uniquely by $J = l$ and $\pi = (-1)^l$. The angular distribution measurement did not allow, however, for the assignment of unique $l$-values. Therefore, the $J^\pi$ assignment for

these states remained ambiguous [KWG94]. The available data are listed in Table 4.1. The resonance strengths in this table were calculated relative to the known 660 keV reference resonance using the relation

$$\omega\gamma = \frac{(2J+1)S_\alpha^l(E_x(P_l(E_\alpha)}{(2J_{ref}+1)S_\alpha^l(E_x^{ref}(P_l(E_\alpha^{ref})}\omega\gamma_{ref} \tag{4.1}$$

where $S_\alpha^l$ is the $\alpha$-spectroscopic factor and $P_l$ the penetrability through the Coulomb and orbital momentum barriers. The uncertain spin assignments for one single resonance create large variations in the corresponding calculated resonance strengths, emphasizing the need to measure the resonances directly. An attempt was made by Vogelaar *et al.* [Vog90] using four large-volume NaI detectors in $4\pi$ geometry and by Giesen *et al.* [Gie94] using a large Ge detector (35%) in close geometry with the target. While the results of the earlier measurement by Trautvetter *et al.* [Tra78] for the resonances above 600 keV were confirmed, the measurements failed in detecting any of the lower resonances. Thus, only upper limits for the strengths of the low energy resonances could be obtained in these experiments (Table 4.1).

**Table 4.1: Low energy resonance parameters found in the literature.**

| | | | | $\omega\gamma$ ($\mu$eV) | | |
|---|---|---|---|---|---|---|
| $E_\alpha(keV)$ | $E_x(MeV)$ | $J^\pi$ | $S_\alpha$ (%) | Using Eq.4.1 | Experimental upper limit | |
| | | | | [KWG94] | [Gie94] | [Vog90] |
| 58 | 9.72 | $3^-$ | 1.1 | $4.1 \times 10^{-40}$ | | |
| | | $(2^+)$ | 2.5 | $1.5 \times 10^{-39}$ | | |
| 218 | 9.85 | $2^+$ | 1 | $7.1 \times 10^{-12}$ | | |
| | | $(1^-)$ | 2.7 | $5.8 \times 10^{-11}$ | | |
| 470 | 10.05 | $0^+$ | 15 | 0.55 | < 1.7 | < (0.0±0.2) |
| | | $(1^-)$ | 4.7 | 0.23 | | |
| 566 | 10.13 | $4^+$ | 0.85 | $7.9 \times 10^{-3}$ | < 1.7 | < (2.0±0.5) |
| | | $(2^+)$ | 1.9 | 1.95 | | |
| | | $(3^-)$ | 1 | 0.15 | | |
| 662* | 10.21 | $1^-$ | 3.5 | 230±25 | | |

*Reference resonance.

## 4.2 Current measurement of the weak resonances

### 4.2.1 The 566 keV resonance

$Al_2O_3$ targets 95 $\mu$g/cm$^2$ in thickness (corresponding to 120 keV energy loss of the $\alpha$-beam at 600 keV) have been used in search of the resonances below 600

keV, using the promising coincidence procedures described above. Typical $\alpha$-beam currents of $\sim$100 $\mu$A on target at energies of 600, 620 and 640 keV have been used to measure a reported resonance at 566 keV [Gie94]. Background measurements have been carried out at $E_\alpha$ = 620 keV using natural oxygen $Al_2O_3$ targets of the same thickness. At lower energies ($E_\alpha$=530 keV), the beam current was limited to about 50 $\mu$A due to increasing instabilities in the operation of the accelerator. This affected the additional attempt to measure the second resonance reported at 470 keV. Details about different runs using both $^{18}O$ and natural oxygen targets are summarized in Table 2.2.

The coincidence spectrum (BGO window 3-11 MeV) for the combined runs at 600, 620 and 640 keV (87.5 C) is shown in the lower panel of Fig. 4.1. It illustrates the clear and unambiguous detection of the 1274 keV transition from the first excited state to the ground state which has never been detected before. The upper panel of the figure shows the spectrum for the same runs but for which only the cosmic ray background component is suppressed. The $\gamma$-lines appearing in this spectrum correspond to those background contributions identified in Section 2.5. The region of the spectrum around the 1274 keV line is further illustrated in Fig. 4.2 for the low-energy resonance as well as for the corresponding background spectrum (31 C) acquired at $E_\alpha$ = 620 keV using the natural oxygen target. For each case, the figure again compares the coincidence spectrum to the spectrum with only cosmic background suppression. This comparison (Figs. 4.1 & 4.2) demonstrates how the real events immersed in the overwhelming room background are "picked out" by making use of the coincidence option. On the other hand, and as a result of the discussion in Subsection 3.2.2, the addback mode instead of the direct mode is chosen for analyzing the coincidence spectra. This proved to be useful in maximizing the coincidence yield with minimum fluctuations due to the addback summing effects.

The net counts under the 1274 keV line in this addback coincidence spectrum (3-11 MeV window in any BGO energy output) of 174.2$\pm$23.7 for the combined measurements of 87.5 C total charge (212.9 hours of beam-time on target), yields an average of 1.99$\pm$0.27 counts per 1 C. The "net" counts are calculated by first subtracting the normalized room background from both "active" and "background with beam" spectra, then subtracting the second result from the first after charge normalization.

At this point, the experimental reaction yield should be translated into a physical resonance strength. As a first estimate, Eq. 3.2 has been used to calculate the strength of the 566 keV resonance relative to the high energy reference resonances by using the net counts under the 1274 keV line in the coincidence spectra. The results listed in the second column of Table 4.2 exhibit significant differences since this analysis does not include the correction factors for the anticipated feeding of the first excited state in the different decay modes. The subsequent analysis (third column of Table 4.2) provides a lower

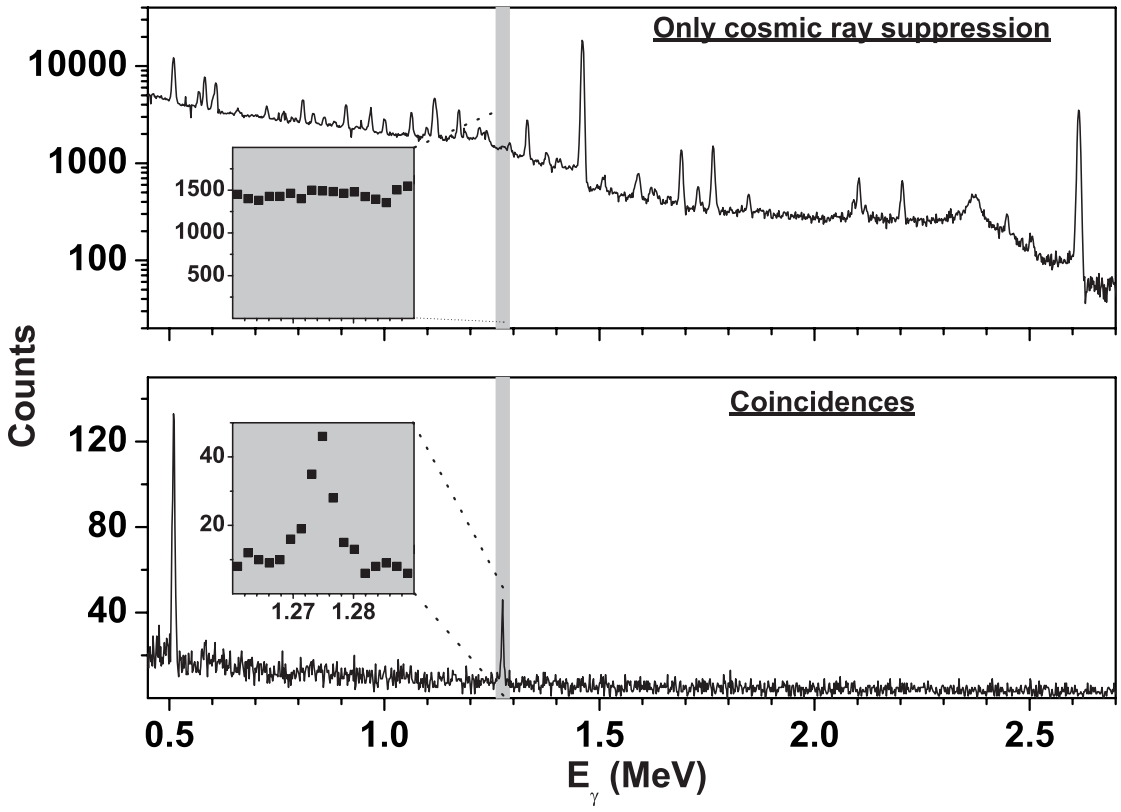


**Figure 4.1: The upper panel shows the spectrum for the combined runs at $E_\alpha$ = 600, 620 and 640 keV with 87.5 C total integrated current and 213 hours of beam time on target. These runs were carried out in search of the weak resonance at 566 keV. The secondary cosmic ray background component is suppressed in this spectrum and the appearing $\gamma$-lines correspond to the background contributions identified in Section 2.5. The shaded area represents the energy region were the first excited state transition is expected. The corresponding coincidence spectrum is shown in the lower panel, which illustrates the strong improvement of the peak-to-background ratio allowing the clear detection of the 1274 keV transition in the very weak 566 keV resonance.**

limit for the resonance strength by including the known bypass correction for the reference resonance (Fig. 3.6) and assuming absolute (100%) decay of the low energy resonance through the first excited state. This calculation yields a lower limit because it assumes no bypasses, which if they exist would indicate missing decays that are not accounted for. It should be emphasized here that this lower limit is not due to statistical uncertainties but rather indicates a real physical lower limit. This lower limit, as calculated from the coincident hits, has of course its own uncertainties which are considered in the table.

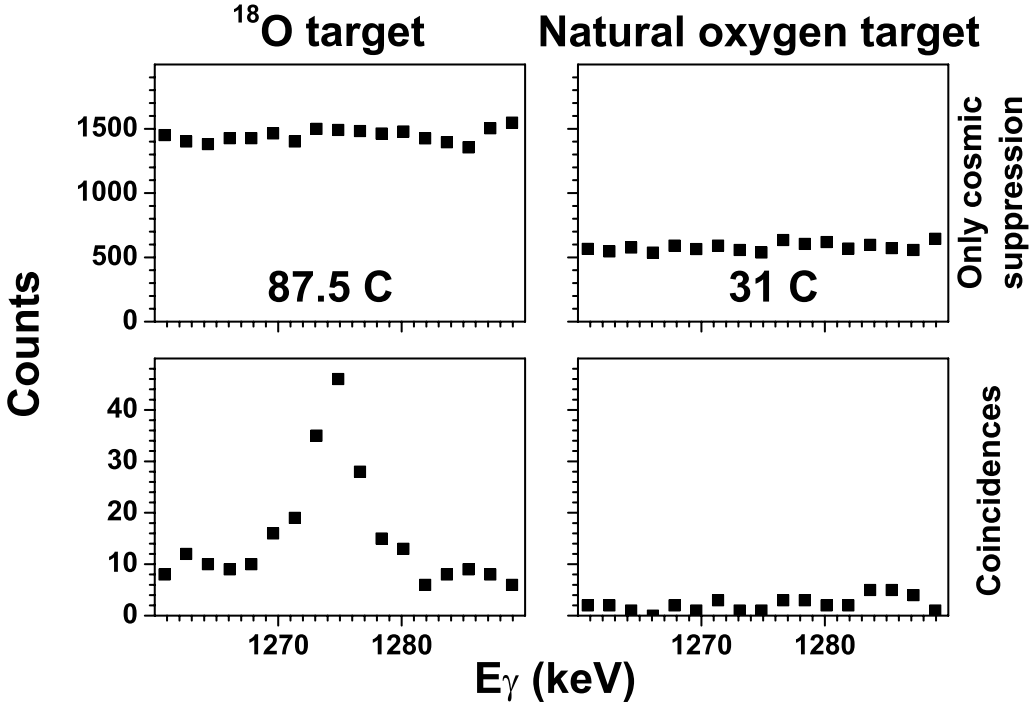


**Figure 4.2: Coincidence option applied to the low energy resonance (566 keV) as well as to the background with beam spectrum. Shown also are the corresponding spectra with only cosmic ray background suppression. The first excited state to ground state transition for the 566 keV resonance can be clearly identified in the coincidence spectrum. All spectra are in addback mode.**

Clearly, the variation in the calculated uncorrected low energy resonance strength demonstrates the necessity for the bypass correction. On the other hand, the calculated lower limits agree very well within the error. This not only confirms the validity of the bypass hypothesis but provides a reliable lower limit for the reaction rate as well.

Up to this point, the available information about the strength of the low energy resonance obtained from direct comparison between coincidence spectra is either not corrected for bypasses, or provides lower limits. The question of proper correction for the resonance strength is still open. Attempts to answer this question are discussed in what follows.

The rather wide BGO coincidence window used so far (3-11 MeV) masks the information about the distribution of the coincident events. A more detailed coincidence analysis is summarized in Fig. 4.3. It shows the distribution of first excited state to ground state coincidence hits with 1 MeV energy windows in the BGO spectrum. By examining this figure as well as the decay modes of the 3 high energy resonances (Fig. 3.6), the first conclusion that can be drawn

**Table 4.2: Strength $\omega\gamma$ of the 566 keV resonance determined relative to the resonances at higher energies. The lower limit is calculated by applying the bypass correction for the reference resonance and assuming no bypasses for the low energy resonance.**

| | $\omega\gamma$ for the 566 keV resonance ($\mu eV$) | |
|---|---|---|
| Reference resonance energy (keV) | No Bypass correction | Lower limit |
| 660 | 3.76±0.66 | 1.04±0.18 |
| 750 | 2.02±0.36 | 1.02±0.18 |
| 770 | 1.04±0.18 | 0.92±0.16 |
| | Average lower limit | 1.0±0.3 |

is the exclusion of the 660 keV resonance as a 'direct' reference for determining the strength of the 566 keV resonance. The distribution profile of the 566 keV resonance shows coincidences in the 3-6 MeV region indicative of the existence of decay modes through intermediate states in contrary to the 660 keV resonance ($J^\pi = 1^-$). This means that among the uncorrected relative strengths of the 566 keV resonance listed in the second column of Table 4.2 one can exclude the highest value of 3.76±0.66 $\mu$eV determined relative to the 660 keV resonance. The relatively large uncertainties in the 566 keV resonance profile (Fig. 4.3 b) do not allow to further adopt or exclude either the 750 or 770 keV resonances as a potential direct reference. It is worth noticing here, however, that though the mode 1 contributions to the total decays differ significantly for the 750 and 770 keV resonances (Table 3.3), mode 1 when compared to the total decays that pass through the first excited state is comparable for both resonances (57.2±8.6 % for the 750 keV resonance and 64.0±6.1 for the 770 keV resonance). Fig.4.3 b shows that the low energy resonance exhibits a similar behavior.

The exact estimation of the "$B$" factor for the 566 keV resonance seems to be not feasible in this way. Alternatively, looking at the problem in a different manner, another approach should be used in order to decide which one of the two remaining high energy resonances, after exclusion of the 660 keV resonance, is preferred as a reference resonance. Recalling the three dimensional matrix coincidence spectra calculated for the high energy resonances (Fig. 3.9) and the clear feature seen for the 750 keV resonance, which is related to the anticipated strong mode 3 transitions, it is therefore worth examining the low energy resonance in the same manner (Fig. 4.4). The three dimensional mode 3 coincidence feature that is clear for the 750 keV resonance is weaker in both the 770 keV and the low energy resonance matrices. Thus, it is most likely that the low energy resonance decay scheme is analogous to the 770 keV resonance which implies maximum feeding of the first excited state.

Accordingly, the net number of coincident events in the 3-MeV × 3-MeV area

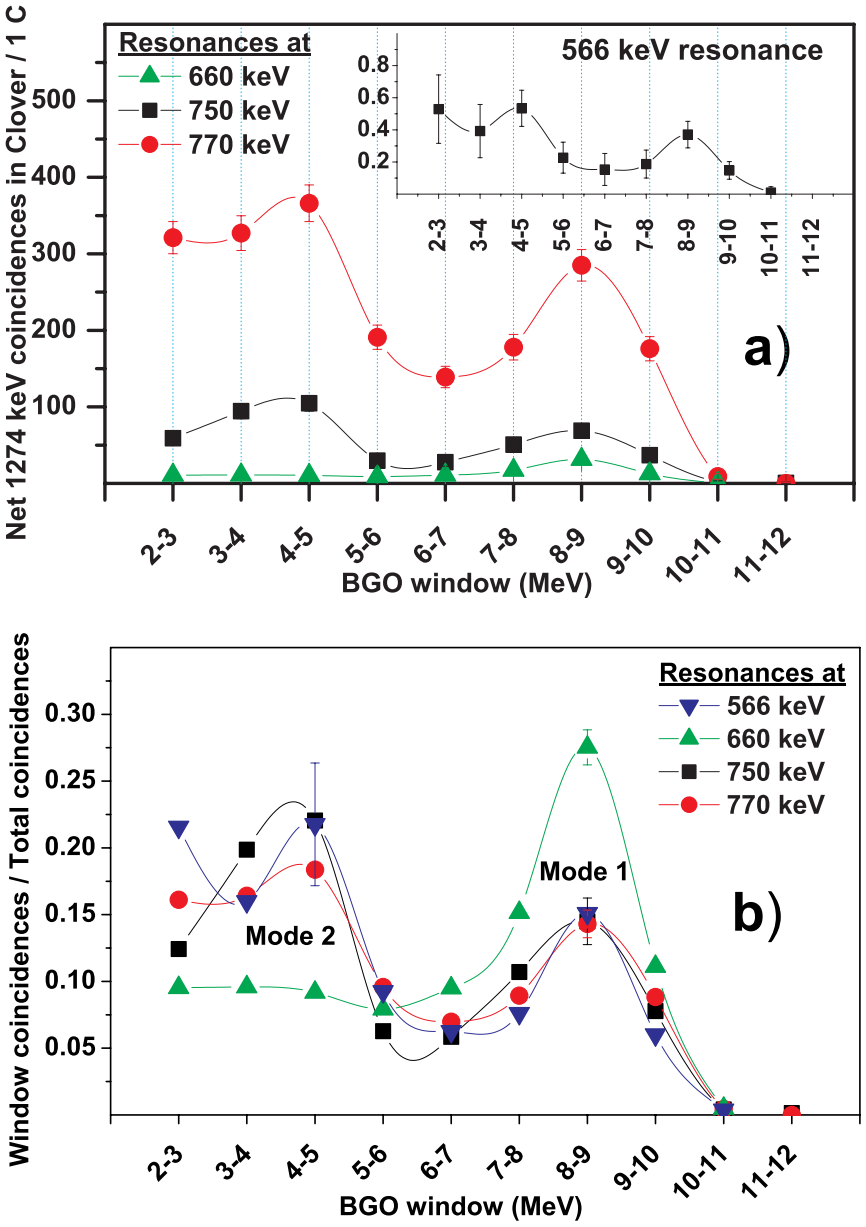


**Figure 4.3: a) Net counts under the 1274 keV line in coincidence with 1 MeV BGO windows. b) The number of coincidences in a 1 MeV window as a fraction to the total number of coincidences in the 2-12 MeV energy region.**

(defined on page 42) of Figs. 3.9 & 4.4 has been calculated and compared to the net 1274 keV gammas that are in coincidence with a 3-11 MeV BGO window (modes 1 & 2). The results are shown in Fig. 4.5 which again favor the 770 keV

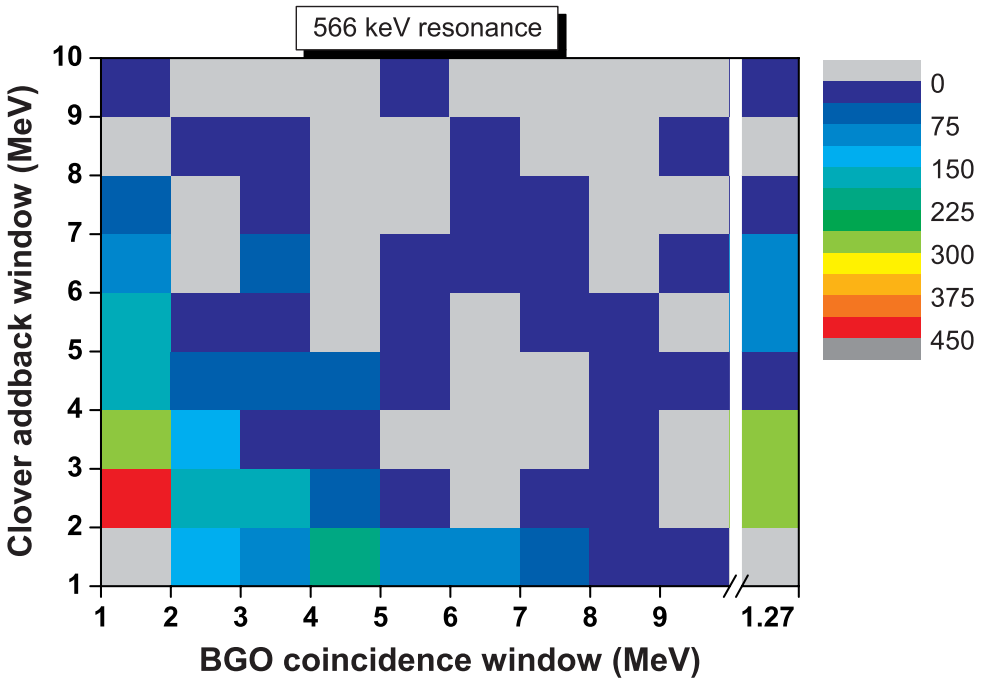


**Figure 4.4: Matrix spectrum for the 566 keV resonance.**

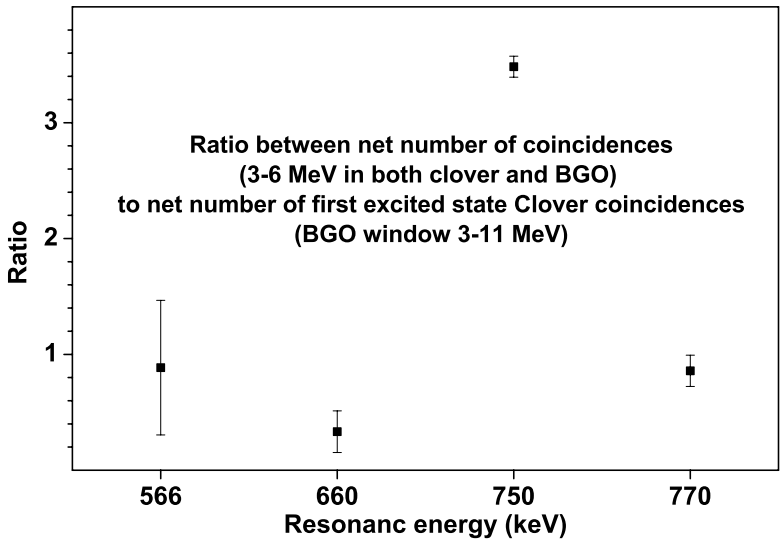


**Figure 4.5: Mode 3 decays compared to transitions through the first excited state (modes 1 & 2) for the 566 keV resonance and the reference resonances.**

resonance as a reference to calculate the strength of the low energy resonance. This means that the resonance strength is indeed $\omega\gamma$=1.04$\pm$0.18 $\mu$eV, whereas $\omega\gamma$=0.7 $\mu$eV can be considered as a conservative lower limit.

### 4.2.2 The 470 keV resonance

As mentioned before, the attempt to directly measure the low energy resonance at 470 keV has been affected by the lower beam currents which was limited to $\sim$50 $\mu$A at $\alpha$-particle energies of 530 keV. The coincidence spectrum obtained at this energy is shown in Fig. 4.6. As for the 566 keV resonance, the uncorrected strengths for the 470 keV resonance as well as its lower limits have been calculated relative to the three reference resonances at higher energies. The results are listed in Table 4.3. Further detailed coincidence analyses like those applied for the 566 keV resonance, *i.e.* the net 1274 keV events in coincidence with 1 MeV BGO windows (like Fig. 4.3) and the matrix spectrum (like Figs. 3.9 & 4.4) have been found not possible due to the large uncertainties. This leaves the question for a preferred reference resonance unanswered. The only hint in this context could come from spin assignments deduced from angular distributions of $\alpha$-transfer reactions [Gie94]. The "net" counts under the 1274 keV line in coincidence with a 3-11 MeV BGO window are 0.37$\pm$0.34 per Coulomb. When compared to the 750 keV resonance (both reported $\boldsymbol{J}^{\pi}$=$0^{+}$ states) without bypass correction, the calculated resonance strength is $\omega\gamma$=0.31$\pm$0.28 $\mu$eV with an upper limit of 0.59 $\mu$eV.

**Table 4.3: Strength $\omega\gamma$ of the 470 keV resonance determined relative to the high energy resonances. The lower limit is calculated by applying the bypass correction for the reference resonance and assuming no bypasses for the low energy resonance.**

| | $\omega\gamma$ for the 470 keV resonance ($\mu eV$) | |
|---|---|---|
| Reference resonance energy (keV) | No Bypass correction | Lower limit |
| 660 | 0.57$\pm$0.53 | 0.16$\pm$0.15 |
| 750 | 0.31$\pm$0.28 | 0.16$\pm$0.14 |
| 770 | 0.16$\pm$0.15 | 0.14$\pm$0.13 |
| | Average lower limit | 0.15$\pm$ 0.24 |

It should be noted, however, that the lower limits calculated relative to the three different reference resonances assuming no bypasses for the 470 keV resonance again agree very well despite the large uncertainties that accompany them.

The rather conservative determination of the "net" counts under the 1274 keV line considered above is achieved by first subtracting normalized room

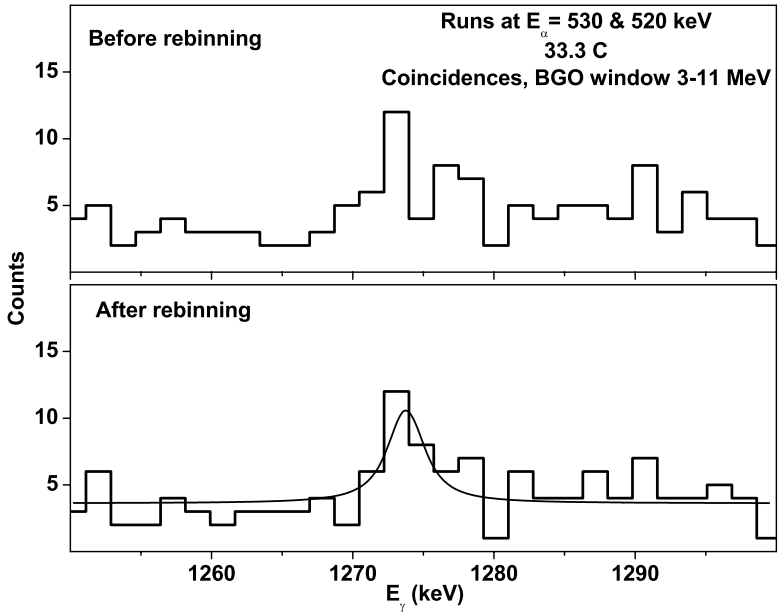


**Figure 4.6: Search for the 470 keV resonance. Shown is the coincidence spectrum (window 3-11 MeV) with and without rebinning (see Subsection 2.3.1). The counting statistics are limited because of the low beam current. The curve is a fit of the 1274 keV transition.**

background from both "active" and "background with beam" spectra, then subtracting the second result from the first after charge normalization. However, the statistical uncertainty could be exaggerated in this approach due to the stepwise normalization and background subtraction processes.

Alternatively, the average number of counts per channel has been computed for the continuum of the rebinned spectrum (Fig. 4.6) in the energy region adjacent to the peak position. The clear feature in this spectrum, which corresponds to the 1274 keV transition, was never seen before. The background corrected net area of this line of 0.50±0.23 per 1 C of integrated current yields a resonance strength of 0.4±0.2 $\mu$eV when compared to the 750 keV resonance. This result is in agreement with the upper limit of 0.61 $\mu$eV obtained from the conservative determination of the resonance strength. Accordingly, the resonance strength of 0.4±0.2 $\mu$eV obtained from Fig. 4.6 will be adopted further on.

The estimates found in the literature for the strength of this resonance suffer from large discrepancies (Table 4.1). This applies in particular to the upper limits reported by [Gie94] and [Vog90] of <1.7 and <(0.0±0.2) $\mu$eV, respectively. The estimates obtained from the angular distribution of the $^{18}$O($^{6}$Li,d)$^{22}$Ne transfer reaction [KWG94] agree, however, with the present measurement.

Given the excellent performance of the present setup and the remarkable

stability of the sputtered targets, there is a good chance to arrive at an improved quantitative result for the 470 keV resonance, if the measurement is repeated at a dedicated facility, where high $\alpha$-beam currents can be realized at low energies as well.

# Chapter 5

# ASTROPHYSICAL IMPLICATIONS

## 5.1 Stellar reaction rates

Because of the fairly high level density, the stellar rate of the $^{18}$O($\alpha$,$\gamma$) reaction is entirely determined by single resonances, while the nonresonant reaction component can be neglected [CF88, Gie94, KWG94, NACRE99]. For a given temperature, the stellar reaction rate per particle pair for a narrow resonance is [Rol88]

$$< \sigma v >= \left(\frac{2\pi}{\mu kT}\right)^{3/2} \hbar^2 \left(\omega\gamma\right)_R \exp\left(\frac{-E_R^{cm}}{KT}\right). \tag{5.1}$$

For several narrow resonances, the total reaction rate is simply the sum over the contributions of the single resonances. In units of reactions per $s^{-1}mol^{-1}cm^3$, the reaction rate as a function of temperature $T_9$ is [KWG94]

$$N_A < \sigma v >= 1.54 \times 10^5 \left(\mu T_9\right)^{-3/2} \sum_i \left(\omega\gamma\right)_i \exp\left(\frac{-11.604 E_{Ri}^{cm}}{T_9}\right), \tag{5.2}$$

where $E_{Ri}^{cm}$ are the center of mass energies of the resonances in MeV, $\left(\omega\gamma\right)_i$ are the corresponding resonance strengths (in eV) and $\mu$ is the reduced mass (in amu).

Before estimating the effect of the resonance strengths obtained in this work (Section 4.2), the stellar reaction rates resulting from previous data (Section 4.1) are reproduced using Eq.5.2. This helps in understanding the relative contribution of resonances with different energies and strengths to the total reaction rate, as well as in providing the ground to compare the experimentally determined rates of this work to the literature estimates.

Fig. 5.1 shows the contribution of the various resonances to the total reaction rate using the resonance strengths tabulated in Table 4.1 (from [KWG94]). The rate reported by [NACRE99] is close to that listed in [KWG94]. The CF88 rate is also indicated in the figure. At high temperatures ($T_9 \geq 0.3$), the reaction rate is determined by the 660 keV and higher energy resonances. In the temperature range of stellar He burning scenarios ($T_9$ = 0.1-0.3), the rate is

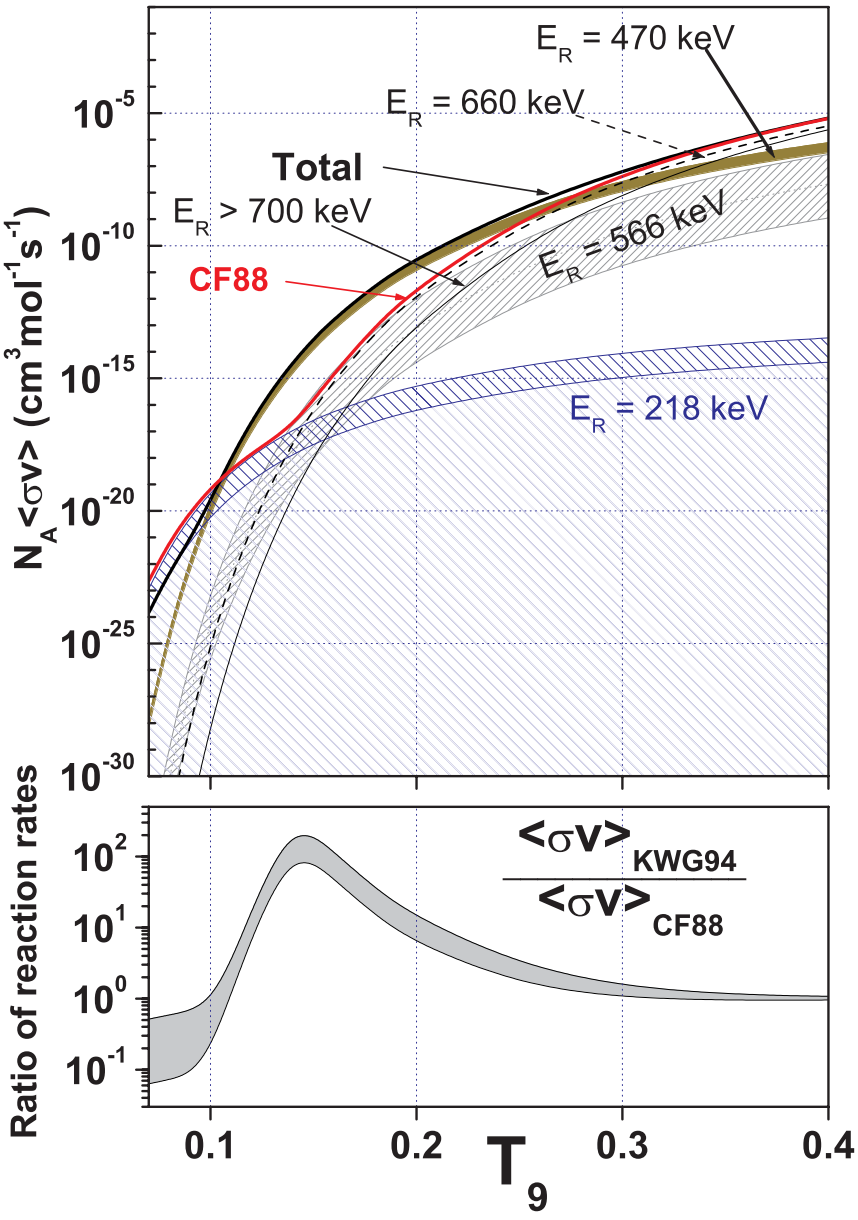


**Figure 5.1: Contribution of single resonances to the reaction rate. The rate is re-calculated using resonance strengths tabulated in Table 4.1 and taken from [KWG94]. Also shown is the CF88-rate. The ratio between both rates is depicted in the lower panel. The shaded areas represent the uncertainties due to the different possible spin assignments as discussed in Section 4.1.**

dominated by the low energy resonances (below 600 keV). The ratio between the [KWG94] and [CF88] rates is depicted in the lower panel. The striking

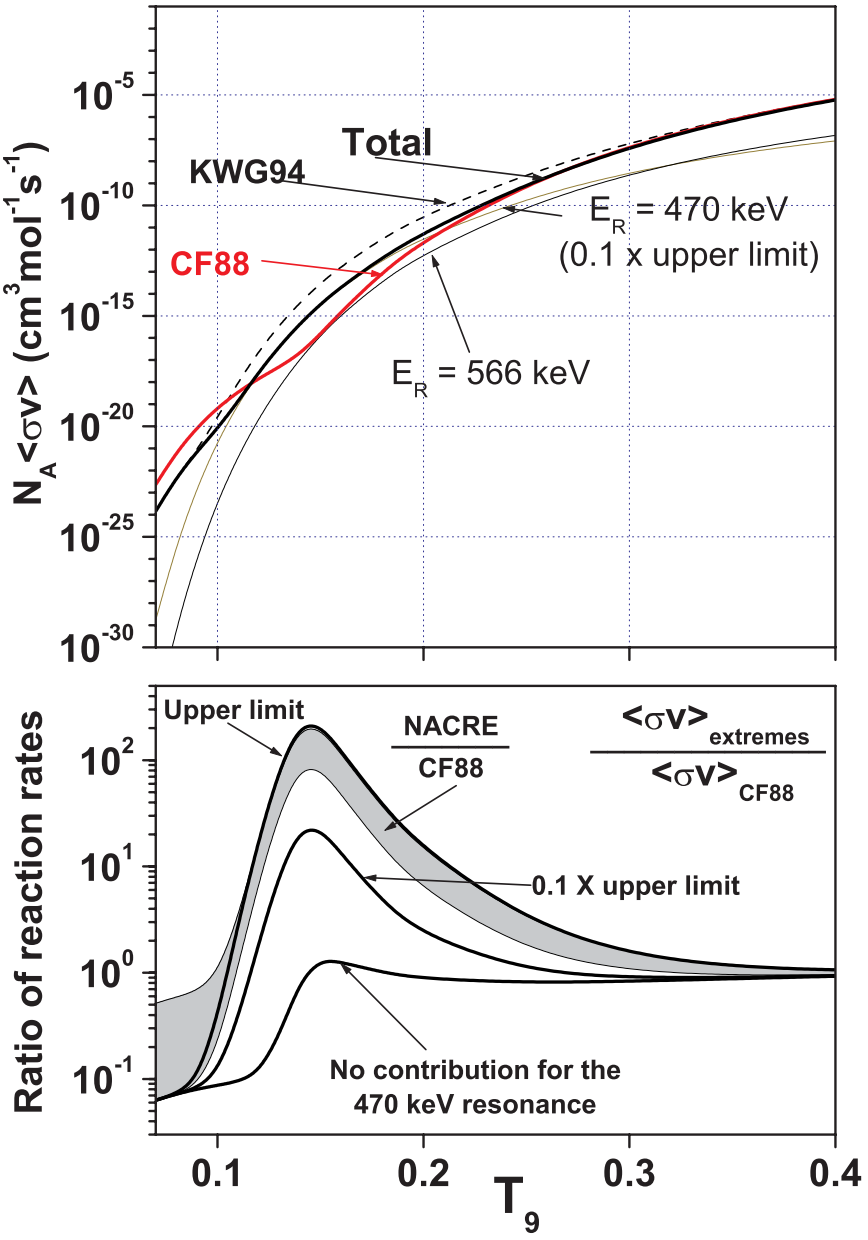


**Figure 5.2: The far extremes of the reaction rate.**

discrepancy is due to the estimated strengths of the low energy resonances at 470 and 566 keV, while the uncertainties represented by the shaded area are related to the different spin assignments. Clearly, the rate is much more sensitive to the 470 keV resonance than to the 566 keV resonance. It should be noted, however, that from the angular distribution of the transfer reaction [Gie94], the spin assignment for the level corresponding to the 566 keV reso-

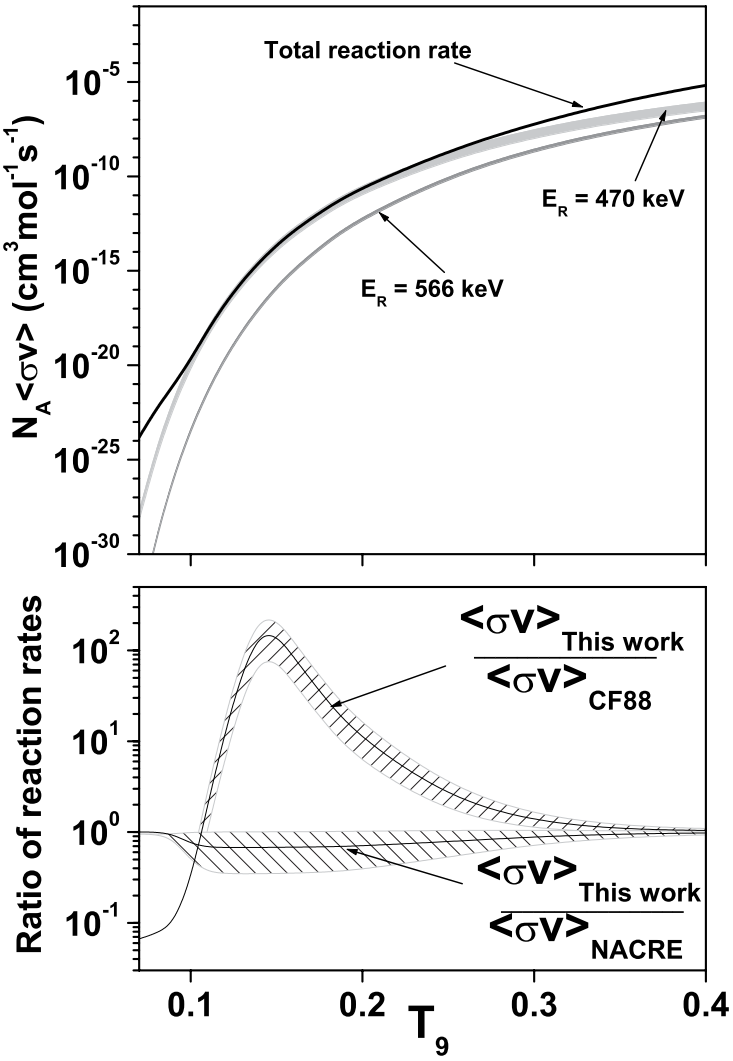


**Figure 5.3: Stellar reaction rates calculated in this work and compared to the literature. The width of the shaded bands in the upper panel represent the uncertainty in the contribution of the 470 and 566 keV resonances. Also shown in the upper panel is the recommended total reaction rate. The rate deduced in this work is compared to the literature in the lower panel and the corresponding uncertainty is represented by the dashed areas.**

nance could indeed be $J^{\pi}=2^{+}$ instead of $4^{+}$ as adopted by [KWG94]. In this case the resonance strength would be 1.95 $\mu$eV instead of $7.9\text{x}10^{-3}$ $\mu$eV, resulting in a more significant contribution to the reaction rate. This argument is indeed supported by the results of the present measurement (Section 4.2). Recalling the lower limits of Table 4.2 for the 566 keV resonance and its average value

of 1.0±0.3 $\mu$eV along with the recommended value of 1.04±0.18 $\mu$eV obtained by comparison with the 770 keV reference resonance, we can thus exclude the $J^{\pi}$=4$^{+}$ assignment and confirm the 2$^{+}$ character of this resonance. The upper limit of (2.0±0.5) $\mu$eV suggested by [Vog90] (Table 4.1) also supports this conclusion.

**Table 5.1: The total reaction rate (cm$^3$mol$^{-1}$s$^{-1}$) and the contribution of the 470 and 566 keV resonances as a function of temperature T$_9$ (=10$^9$K).**

| T$_9$ | 470 keV | 566 keV | Total | T$_9$ | 470 keV | 566 keV | Total |
|---|---|---|---|---|---|---|---|
| 0.07 | 1.20E-28 | 6.78E-34 | 1.53E-24 | 0.70 | 3.10E-05 | 2.14E-05 | 3.88E-03 |
| 0.08 | 2.83E-25 | 8.14E-30 | 5.08E-23 | 0.80 | 5.63E-05 | 4.58E-05 | 1.09E-02 |
| 0.09 | 1.16E-22 | 1.19E-26 | 8.66E-22 | 0.90 | 8.77E-05 | 8.09E-05 | 2.40E-02 |
| 0.10 | 1.41E-20 | 3.97E-24 | 2.05E-20 | 1.00 | 1.23E-04 | 1.25E-04 | 4.45E-02 |
| 0.11 | 7.08E-19 | 4.55E-22 | 7.45E-19 | 1.25 | 2.15E-04 | 2.63E-04 | 1.36E-01 |
| 0.12 | 1.82E-17 | 2.34E-20 | 1.84E-17 | 1.50 | 2.96E-04 | 4.09E-04 | 3.64E-01 |
| 0.13 | 2.83E-16 | 6.49E-19 | 2.84E-16 | 1.75 | 3.60E-04 | 5.42E-04 | 1.24E+00 |
| 0.14 | 2.93E-15 | 1.11E-17 | 2.95E-15 | 2.00 | 4.05E-04 | 6.51E-04 | 4.39E+00 |
| 0.15 | 2.21E-14 | 1.29E-16 | 2.23E-14 | 2.50 | 4.52E-04 | 7.97E-04 | 3.22E+01 |
| 0.16 | 1.29E-13 | 1.10E-15 | 1.31E-13 | 3.00 | 4.63E-04 | 8.68E-04 | 1.26E+02 |
| 0.18 | 2.40E-12 | 3.86E-14 | 2.49E-12 | 3.50 | 4.55E-04 | 8.89E-04 | 3.34E+02 |
| 0.20 | 2.44E-11 | 6.51E-13 | 2.66E-11 | 4.00 | 4.37E-04 | 8.82E-04 | 6.86E+02 |
| 0.25 | 1.51E-09 | 1.00E-10 | 2.30E-09 | 5.00 | 3.90E-04 | 8.25E-04 | 1.85E+03 |
| 0.30 | 2.25E-08 | 2.74E-09 | 6.51E-08 | 6.00 | 3.45E-04 | 7.51E-04 | 3.53E+03 |
| 0.35 | 1.50E-07 | 2.81E-08 | 8.95E-07 | 7.00 | 3.04E-04 | 6.77E-04 | 5.53E+03 |
| 0.40 | 6.03E-07 | 1.57E-07 | 7.01E-06 | 8.00 | 2.70E-04 | 6.10E-04 | 7.68E+03 |
| 0.45 | 1.74E-06 | 5.85E-07 | 3.59E-05 | 9.00 | 2.40E-04 | 5.51E-04 | 9.84E+03 |
| 0.50 | 4.01E-06 | 1.65E-06 | 1.34E-04 | 10.0 | 2.16E-04 | 4.99E-04 | 1.19E+04 |
| 0.60 | 1.35E-05 | 7.51E-06 | 9.61E-04 | | | | |

The results obtained for the 470 keV resonance, on the other hand, can not be interpreted so easily. As discussed before, the uncertainties due to the weak beam currents attainable at 530 keV do not allow for a reasonably precise conclusion about the resonance strength. This resonance strongly influences the reaction rate at the temperatures of interest. Unfortunately, though the coincidence method has proved to be effective in solving the ambiguity in the 566 keV resonance, the measurement of the weaker resonance at 470 keV remained unsatisfactory.

Cases when only upper limits are available for a given resonance are sometimes treated in the literature by assuming 10% of the upper limit for an estimate of the resonance strength [CF88, NACRE99]. From our conservative result of 0.31±0.28 $\mu$eV for the strength of the 470 keV resonance we can use the upper limit multiplied by 0.1, *i.e.* 0.06 $\mu$eV. The lower limit simply corresponds

to a non-populated resonance. Fig. 5.2 shows those far extremes compared to [CF88].

On the other hand, we have obtained a value of 0.4±0.2 $\mu$eV for the strength of this resonance by analyzing the rebinned spectrum (see Fig. 4.6 and the related discussion in Section 4.2). The more realistic rate based on this result is shown in Fig. 5.3. In this calculation, the above mentioned resonance strength has been considered for the contribution of the 470 keV resonance and the uncertainty is represented by the shaded area in the upper panel of the figure. Comparison with the literature is shown in the lower panel. The present rate confirms the strong enhancement (relative to Caughlan and Fowler [CF88]) at He burning temperatures suggested by [KWG94] and by the NACRE compilation [NACRE99].

The total reaction rate and the contributions of the 470 and 566 keV resonances are also given in tabular form (Table 5.1). The temperature steps are the same as in [CF88] and [NACRE99].

The analytical approximation for the contribution of both low-energy resonances at 470 and 566 keV is

$$N_A < \sigma v >_{470,566} = 1.07 \times 10^{-2} T_9^{-3/2} exp(-4.462/T_9)$$
$$+2.70 \times 10^{-2} T_9^{-3/2} exp(-5.373/T_9), \quad (5.3)$$

where the rate is again given in cm$^3$mol$^{-1}$s$^{-1}$. Hence, the total reaction rate for $T_9 \leq 6$ is given by

$$N_A < \sigma v > = 1.95 \times 10^{-13} T_9^{-3/2} exp(-2.069/T_9)$$
$$+1.07 \times 10^{-2} T_9^{-3/2} exp(-4.462/T_9) + 2.70 \times 10^{-2} T_9^{-3/2} exp(-5.373/T_9)$$
$$+10.1 T_9^{-3/2} exp(-6.391/T_9)$$
$$+44.1 T_9^{-3/2} exp(-7.389/T_9)$$
$$+3.44 \times 10^{5} T_9^{-0.5} exp(-22.103/T_9). \quad (5.4)$$

The exponential term in Eq. 5.1 implies that resonances with energies near kT will determine the reaction rate for a given stellar temperature [Rol88]. For temperatures of stellar He burning, the energies and strengths of the low-energy resonances are, therefore, extremely important. In particular, the 470 keV resonance dominates in this temperature region (see Table 5.1). This underlines the importance of an additional measurement with improved beam current for defining the strength of this resonance more accurately. In using the coincidence technique for the detection of primary transitions, this improvement is expected to yield the exact determination of the resonance energy.

## 5.2 Fate of $^{18}$O during stellar He burning

As indicated in Chapter 1, the $^{14}$N ashes of hydrogen burning are converted to $^{22}$Ne by the reaction sequence $^{14}$N($\alpha$,$\gamma$)$^{18}$F($\beta^+$)$^{18}$O($\alpha$,$\gamma$)$^{22}$Ne. The efficiency of the subsequent $^{22}$Ne($\alpha$,n)$^{25}$Mg neutron source for the *s* process thus depends on the preceding $\alpha$ capture reactions.

**Figure 5.4: The ratio of the stellar rates for the $^{18}$O($\alpha$,$\gamma$)$^{22}$Ne reaction obtained in this work and $^{18}$O($\alpha$,n)$^{21}$Ne reaction taken from [CF88]. The ratio obtained from [CF88] data for both reactions is shown for comparison.**

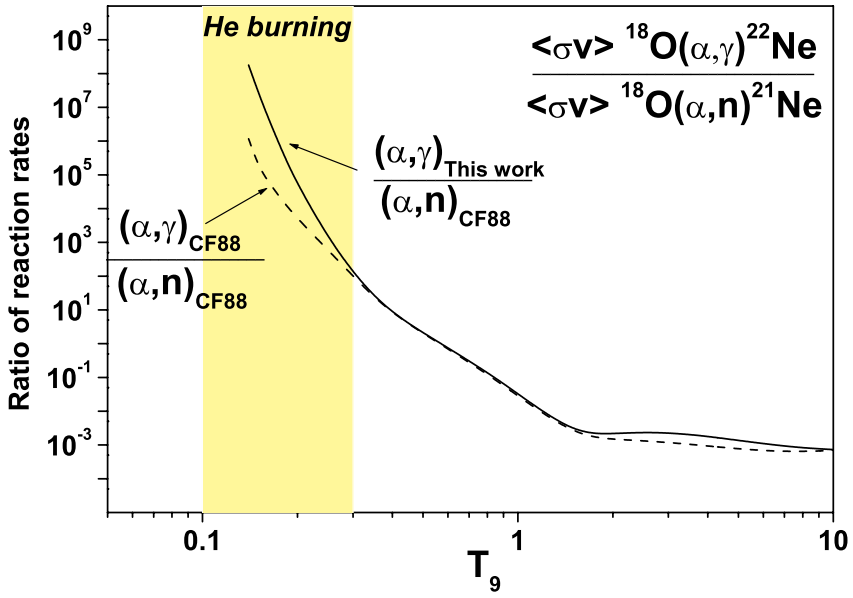


The improved reaction rates obtained in the present work represent a significant step in understanding the fate of $^{18}$O nuclei during stellar He burning. The production of $^{22}$Ne clearly depends on the relative reaction cross sections for the competing $^{18}$O($\alpha$,$\gamma$)$^{22}$Ne and $^{18}$O($\alpha$,n)$^{21}$Ne reactions. The relevant Q-values are $Q_{\alpha\gamma}$ = 9.67 MeV and $Q_{\alpha n}$ = -0.70 MeV. Figure 5.4 depicts the ratio between the reaction rates for both processes. The data confirm the clear domination of the ($\alpha$,$\gamma$) channel leading to $^{22}$Ne production at the temperatures of stellar He burning. The strengths of the low energy resonances measured in this work are strongly enhancing this production and are, hence, important for defining the respective time scale for activating the subsequent $^{22}$Ne($\alpha$,n)$^{25}$Mg neutron source for the *s* process. This confirms the conclusions of [Gie94].

It should be emphasized, however, that earlier values of the low energy resonance strengths [KWG94, Gie94, Vog90] and consequently the reaction rates were based on theoretical estimates or experimental upper limits. The direct experimental measurement of these extremely weak resonances, which are the

weakest ever detected, puts these conclusions concerning the relevant astrophysical consequences now on firm grounds. The detailed influence of the present rates on the reaction flow and the time evolution of the $^{22}$Ne abundance as well as on the neutron balance in stellar He burning can now be worked out using the reaction network calculations in the frame of stellar model codes.

# Chapter 6

# CONCLUDING REMARKS

The $^{18}$O($\alpha$,$\gamma$)$^{22}$Ne reaction at low energies is of considerable astrophysical interest since it determines the role of the important neutron source $^{22}$Ne($\alpha$,n) for *s*-process nucleosynthesis. However, the astrophysically relevant resonances in this reaction at 566 and 470 keV are difficult to measure due to their extremely low resonance strengths.

The present work describes a successful experimental approach that results in the determination of the strength of the 566 keV resonance with a value 1.0$\pm$0.2 $\mu$eV and of the 470 keV resonance with a value 0.4$\pm$0.2 $\mu$eV. These are the weakest resonances ever directly measured. This experimental success has been achieved by a carefully designed spectrometer, which has been optimized for strong background suppression. The $\gamma$-spectrum has been acquired by a clover-like array of coaxial n-type HPGe detectors in coincidence with energy windows set in BGO scintillators upstream of the target. This combination of the high resolution Ge Clover detector and the high efficiency BGO scintillators was instrumental for achieving the required detection sensitivity for investigating the very weak resonances at astrophysical energies. The remarkable stability of the sputtered targets under the thermal load of high beam currents is an additional parameter contributing to the success of the measurement.

From the measured yield, resonance strengths have been deduced by referring to known resonances at higher energies. Corrections for the different decay schemes of the resonant states have been carefully investigated and are discussed in detail.

Based on these results, the determination of the strength of the 566 keV resonance reduces considerably the previous uncertainties in its contribution

to the total reaction rate. The sensitivity of the present experiment is sufficient to deduce the contribution of the weaker resonance at 470 keV as well. If repeated with $\alpha$-particle beams of an intensity comparable to that used to measure the 566 keV resonance, it is expected that this result can be further improved.

With the experimental results of this work, the reaction rate could be quantified reliably and has been found to be higher compared to previous estimates by Caughlan and Fowler [CF88]. We confirm the strong enhancement at He burning temperatures suggested by [KWG94] and by the NACRE compilation [NACRE99].

# References


[Ada69]

A. Adams, M.H. Shapiro, W.M. Denny, E.G. Adelberger, and C.A. Barnes, Nucl. Phys. **A131** (1969), 430.

[Ant77]

A. Anttila, J. Keinonen, M. Hautala, and I. Forsblom, Nucl. Instr. Meth. **147** (1977), 501.

[$B^2$FH57]

E.M. Burbidge, G.R. Burbidge, W.A. Fowler, and F. Hoyle, Rev. Mod. Phys. **29** (1957), 547.

[CF88]

G.R. Caughlan and W.A. Fowler, Atomic Data Nucl. Data Tables **40** (1988), 283.

[Deb88]

K. Debertin and R.G. Helmer, *Gamma- and x-ray spectrometry with semiconductor detectors*, Elsevier Science Publishers B.V., Amsterdam, 1988.

[Duc99]

G. Duchêne, F.A. Beck, P.J. Twin, G. de France, D. Curien, L. Han, C.W. Beausang, M.A. Bentley, P.J. Nolan, and J. Simpson, Nucl. Instr. Meth. **A432** (1999), 90.

[End90]

P.M. Endt, Nucl. Phys. A **521** (1990), 1.

[Gal98]

R. Gallino, C. Arlandini, M. Busso, M. Lugaro, C. Travaglio, O. Straniero, A. Chieffi, and M. Limongi, Ap. J. **497** (1998), 388–403.

[GEANT4]

Geant4-Collaboration, http://wwwinfo.cern.ch/asd/geant4/geant4.html.

[Gie94]

U. Giesen, C.P. Browne, J. Görres, J.G. Ross, M. Wiescher, R. E. Azuma, J.D. King, and M. Buckby, Nucl. Phys. **A567** (1994), 146.

[Gör00]

J. Görres, C. Arlandini, U. Giesen, M. Heil, F. Käppeler, H. Leiste, E. Stech, and M. Wiescher, Phys. Rev. C **62** (2000), 055801.

[Gör01]

J. Görres, C . Arlandini, U. Giesen, M. Heil, F. Käppeler, H. Leiste, E. Stech, and M. Wiescher, Nucl. Phys. **A688** (2001), 225c.

[Gov60]

H.E. Gove and A.E. Litherland, Nuclear Spectroscopy (F. Ajzenberg-Selove, ed.), Academic Press, New York, 1960, p. 260.

[Jos97]

P.K. Joshi, H.C. Jain, A.S. Medhi, S. Chattopadhyay, S. Bhattacharya, and A. Goswami, Nucl. Instr. Meth. **A399** (1997), 51.

[Jun01]

M. Junker and LUNA-Collaboration, Nucl. Phys. **A688** (2001), 267c.

[Käp89]

F. Käppeler, H. Beer, and K. Wisshak, Rep. Prog. Phys. **52** (1989), 945–1013.

[Käp98]

F. Käppeler, F.-K.. Thielemann, and M. Wiescher, Ann. Rev. Nucl. Part. Sci. **48** (1998), 175–251.

[Käp99]

F. Käppeler, Prog. Nucl. Part. Phys. **43** (1999), 419–483.

[Kno00]

G.F. Knoll, *Radiation detection and measurement*, Wiley, NY, 2000.

[KWG94]

F. Käppeler, M. Wiescher, U. Giesen, J. Görres, I. Baraffe, M. El Eid, C.M. Raiteri, M. Busso, R. Gallino, M. Limongi, and A. Chieffi, Ap. J. **437** (1994), 396–409.

[Lew88]

T.A. Lewis, Nucl. Instr. Meth **A264** (1988), 534.

[Mey94]

B.S. Meyer, Annu. Rev. Astron. Astrophys. **32** (1994), 153–190.

[NACRE99]

C. Angulo, M. Arnould, M. Rayet, P. Descouvemont, D. Baye, C. Leclercq-Willain, A. Coc, S. Barhoumi, P. Aguer, C. Rolfs, and R. Kunz, Nucl. Phys. **A656** (1999), 3, Also available online as NACRE compilation, http://pntpm.ulb.ac.be/nacre.htm.

[NuDat02]

R. Kinsey, *Nudat on the web*, (2002), www.nndc.bnl.gov/nndc/nudat/; National Nuclear Data Center, Brookhaven National Laboratory.

[Pai79]

B.M. Paine and D.G. Sargood, Nucl. Phys. **A331** (1979), 389.

[Rol88]

C. Rolfs and W. Rodney, *Cauldrons in the cosmos*, University of Chicago Press, Chicago, 1988.

[Sco75]

H.L. Scott and T.F. Lusby, Nucl. Instr. Meth. **131** (1975), 517.

[SRIM00]

J.F. Ziegler and J.P. Biersack, SRIM 2000, The Stopping and Range of Ions in Matter, http://www.srim.org.

[Tra78]

H.P. Trautvetter, M. Wiescher, K.U. Kettner, C. Rolfs, and J.W. Hammer, Nucl. Phys. **A297** (1978), 489.

[Vog90]

R.B. Vogelaar, T.R. Wang, S.E. Kellogg, and R.W. Kavanagh, Phys. Rev. C **42** (1990), 753.

[Wie01]

M. Wiescher, Nucl. Phys. **A688** (2001), 241c.

# Acknowledgment

It is indeed a pleasure to acknowledge my thanks to Prof. Dr. H. Rebel for his supervision as well as for providing the opportunity for me to join Forschungszentrum Karlsruhe, where this work has been conducted. Thanks in this regard should go also to Prof. Dr. H. Blümer, head of the Institut für Kernphysik. I am also grateful to Prof. Dr. G. Wolschin for accepting to act as a referee for this work.

Dr. Franz Käppeler, “Danke Schön” can never be enough. His commendable patience, guidance, friendship and perseverance are few among the inexpressibles! No words can phrase my indebtedness.

Special gratitude to Prof. Dr. M. Wiescher for his continuous encouragement, Dr. J. Görres for his detailed involvement and contributions, Dr. U. Giesen for the fruitful discussions and Dr. H. Leiste for providing the sputtered targets.

Dr. K. Wisshak, Dr. F. Voss and Dr. H. Beer, it was great pleasure to join you.

M. Heil, R. Reifarth and all my dear colleagues in the Nuclear Astrophysics group, C. Arlandini, W. Rapp, R. Plag and M. Mosconi, thanks for everything!

How could I forget G. Rupp and his technical support! The accelerator staff, D. Roller, E.-P. Knaetsch and W. Seith. Vielen Dank!

Knowing them all, and working with them, was the most beautiful and ever lasting “coincidence” in this work!

I like to acknowledge the financial support provided under grant Nr. 315/ppp/gü-ab by the Deutscher Akademischer Austausch Dienst (DAAD) for the collaboration between Forschungszentrum Karlsruhe and the University of Notre Dame.

It is my pleasure also to express my deep feelings toward Al Balqa University and my thanks for its support.

My mother, Ramzy, Rula, Rawan, Zein and all those “precious” ones among family and friends, your love was always my first motivation.